NANOMATERIALS FOR ENERGY APPLICATION: PHOTOCATALYTIC HYDROGEN PRODUCTION AND ENHANCED OIL RECOVERY

A Dissertation

by

YI-HSIEN YU

Submitted to the Office of Graduate and Professional Studies of
Texas A&M University
in partial fulfillment of the requirements for the degree of

DOCTOR OF PHILOSOPHY

Chair of Committee,	Zhengdong Cheng
Committee Members,	Perla Balbuena
	Mustafa Akbulut
	Sreeram Vaddiraju
Head of Department,	Ibrahim Karaman

December 2016

Major Subject: Materials Science and Engineering

ABSTRACT

Prediction made by U.S. Energy Information Administration, energy demand will increase more than 40% in next 30 years and renewable energy is the fastest growing energy source at an average increase rate of 2.6%. Although lots of alternative energy sources have been developed, the majority are still from fossil fuels. After primary and secondary oil recovery, 30 - 60% of original oil in place (OOIP) is left in the oil field. Additional oil could be recovered by chemical injection, or an alternative method – nanofluid injection to reduce adverse ecological concerns. The primary objects of this research were aiming at applying nanotechnology for development/modification of existing nanomaterials for energy related applications: photocatalytic hydrogen production and enhanced oil recovery.

One dimensional nanomaterials are considered favorably for electrons transport along axial direction due to the structural configuration. A green, novel, and fast microwave-assisted method was introduced to synthesize one dimensional CuO/TiO_2 rods nanocomposites. Systematic investigation of deposited CuO amount on photocatalytic hydrogen production rate revealed that there was a CuO/TiO_2 optimal ratio that enhanced hydrogen yield rate by 77 times. In addition, chemical vapor deposition was used to synthesize Zn_3P_2 nanowires and provided with in-situ surface functionalization. The surface modifier give Zn_3P_2 nanowires better resistance to moisture and degradation.

Two dimensional nanodisks are able to attach at oil/water interface, known as Pickering emulsion, subsequently formed extremely stable emulsion droplets. ZrP nanodisks fabricated from three synthesis methods, hydrothermal, reflux, and microwave-

assisted, are characterized and evaluated. In addition to fabrication methods, solvent also plays an important role in the synthesis procedure. Selected proper solvent provides a new route to obtain ZrP nanodisks less than 100 nm.

Finally, the nanofluid containing amphiphilic ZrP nanodisks and microfluidic device for enhanced oil recovery was examined. The surface functional groups were served not only as surface modifier, but also capping agent to control the size of ZrP nanodisks in the one-pot synthesis procedure. The surface of ZrP nanodisks can be secondary functionalized to reach higher surface coverage of functional groups and further reduce interfacial tension of oil/water. The results showed oil recovery rate was increased in the presence of ZrP amphiphilic nanodisks.

DEDICATION

To my dear family

ACKNOWLEDGEMENTS

I would like to thank my committee chair, Dr. Zhengdong Cheng, and my committee members, Dr. Perla Balbuena, Dr. Mustafa Akbulut, and Dr. Sreeram Vaddiraju, for their guidance and support throughout the course of this research. I'd like to also thank Dr. Alex Fang for giving me an opportunity to be his TA to learn more fundamental knowledge on non-metallic materials.

Thanks also go to my friends: Bruce Chen, Po-Chun Chen, Alvin Chang, Charles Chen, Dryan Chen, Jerry Huang, Hui-Chin Chiu, Nikki Chen, Chung-Han Chiou, TC Lee, Sin-Hong Lin, Verna Wei, Cassandra Lee, Hung-Long Wei, Jolie Chuang, Stephen Chen, Te-Wei Chen, Jerry Yen, Jerry Yiu, Chin-Hua Cheng and people in Dr. Cheng's group, Dr. Andes Mejia, Dr. Ya-Wen Chang, Dr. Min Shuai, Xuezhen Wang, Minxiang Zheng, Eric Zhang, Abhijeet Shinde, Ilse Nova, Carlos, and the department faculty and staff. Thank you, all, for making my time at Texas A&M University a great experience.

Finally, special thanks to my beloved wife, Fu-Ning Hsu, and my dear family. I could not have made it without their support through the years.

CONTRIBUTORS AND FUNDING SOURCES

Contributors

This work was supervised by a dissertation committee consisting of Professor Zhengdong Cheng, Perla Balbuena, Mustafa Akbulut and Sreeram Vaddiraju of the Artie McFerrin Department of Chemical Engineering.

The Zn_3P_2 sample analyzed in **Chapter II** was kindly provided by Professor Sreeram Vaddiraju. The XRD analyses depicted in **Chapter II and III** were conducted in part by Yin-Ping Chen of the Department of Chemistry and were published in 2015 and 2016. The AAO was donated by Professor Bruce Chen from NTUST.

All other work conducted for the dissertation was completed by the student independently.

Funding Sources

This work was made possible in part by ITF under Grant Number 3382PSD, NSF under Grant Number DMR-1006870, NASA under Grant Number NASANNX13AQ60G, and seed fund support “Solar Energy Harvesting” from the Artie McFerrin Department of Chemical Engineering, Texas A&M University.

TABLE OF CONTENTS

Page

LIST OF FIGURES

Page

LIST OF TABLES

Page

CHAPTER I

INTRODUCTION

1.1 Background

1.1.1 Photocatalytic hydrogen production

To supply of clean and sustainable energy is one of the most challenging tasks in the 21st century. Based on prediction made by U.S. Energy Information Administration, energy demand will increase more than 40% in next 30 years. In 2012, worldwide primary energy consumption was 549 quadrillion British thermal units (Btu) and is projected to rise to 815 quadrillion Btu in 2040 [1]. More than 70% of energy is produced from fossil fuels and only 11% of energy is from renewable energy. It is necessary to develop sustainable energy and to reduce greenhouse gas accumulation as well as to reserve depletion of fossil fuels.

Solar energy is considered as a sustainable energy source with the great potential over other renewable energy resources. The solar energy received on earth is several order higher than annual global energy consumption. However, there are three major factors that limit utilization of solar energy. First, the solar energy could not be directly used and has to be efficiently converted to usable energy forms, such as electricity. Second, the use of solar energy strongly depends on geographic condition, such as weather, daytime, and land availability. Hence, due to the intermittency of solar irradiation, efficient conversion and storage of solar energy are necessary to the end users.

An efficient model system has been shown by nature for conversion and storage of solar energy: the photosynthetic system. People were inspired by nature realizing that

solar energy can be converted and stored in the form of chemical bonds and subsequently be used to produce oxygen and hydrogen from water (shown in Figure 1a and b). In 1972, Fujishima's research opens a window for using semiconductor material to split water into O_2 and H_2 under ultraviolet (UV) irradiation [2]. The water splitting reaction soon attracts attention of researchers for decades due to the highly similarity of photosynthesis by plants. Therefore, water splitting is regarded as an artificial photosynthesis process.

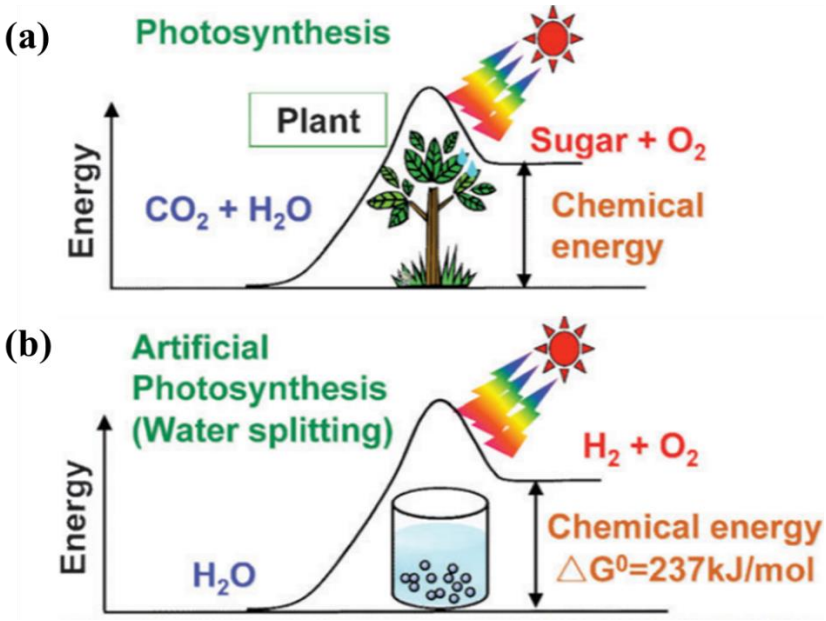

Figure 1. (a) Photosynthesis by green plants, and (b) photocatalytic water splitting as an artificial photosynthesis. Reprinted with permission from Ref. [3]. Copyright The Royal Society of Chemistry**.**

1.1.1.1 Mechanisms of photocatalytic hydrogen production

An electrolytic cell with two electrodes placed in water and connected to electrical power source can be used to realize the reaction of water splitting. When electrical power

is on, the cathode will receive electrons and hydrogen is subsequently generated at the interface of electrode by water reduction reaction. Similarly, oxygen will be produced at the anode by water oxidation reaction. Nernst equation can be applied to calculation of the electrode potential. The total potential to split water is 1.23 volt (V), which is corresponding to the free energy change for the conversion of one molecule of H_2O to H_2 and 1/2 O_2 under standard conditions (ΔG = 237.2 kJ/mol).

Oxygen Evolution Reaction (OER)

$$H_2O \rightarrow \frac{1}{2}O_2 + 2H^+ + 2e^- \quad E^0_{OER} = 1.23 \text{ V vs NHE}$$

Hydrogen Evolution Reaction (HER)

$$2H^+ + 2e^- \rightarrow H_2 \; E^0_{HER} = 0 \text{ V vs NHE}$$

Overall: $H_2O \rightarrow \frac{1}{2}O_2 + H_2 \;\; E = E^0_{OER} - E^0_{HER} = -1.23 \text{ V}$

The requirement for use of semiconductors to drive water splitting reactions with light is that semiconductors are able to provide a voltage larger than 1.23 V. In other words, semiconductors for water splitting must be able to absorb radiant light with photon energies of at least 1.23 electron-volt (eV, equal to wavelengths of ca. 1000 nm) and use the adsorbed energy to split water into H_2 and O_2. Ideally, a semiconductor material with band gap energy (E_g) larger than 1.23 eV and conduction band-edge energy (E_{cb}) more negative than electrochemical potentials $E°$ (H^+/H_2) as well as valence band-edge energy (E_{vb}) more positive than electrochemical potentials $E°$ (O_2/H_2O) is capable of driving

hydrogen evolution reaction (HER) and oxygen evolution reaction (OER) under illumination. However; the model is simply based on thermodynamics and is far from reality. The surface chemistry of semiconductors and kinetics also need to be considered.

During the photocatalytic water splitting, several critical processes and reactions are involved including generation of electron-hole pairs (charge separation), electron-hole recombination (charge recombination), migration of charges, trap of excited charges, and transfer of excited charges to water or other molecules [4]. All of the processes have to be taken into account in order to generate hydrogen efficiently. It is obvious that any step helps to separate/transfer charges would enhance the overall efficiency. Meanwhile, steps that consume/recombine electron-hole pairs need to be avoided. In general, the efficiency of the photocatalyst is substantially affected by two important competing processes: the charge recombination and separation/migration processes. Charge recombination includes surface and bulk recombination, which are both classified as deactivation processes. Charge recombination will be reduced by efficient charge separation and transport, which is fundamentally important for photocatalytic water splitting. Therefore, two conditions are required in the development of high-efficiency semiconductor materials for the water splitting: (a) adequate band gap of photocatalyst to harvest light source and to drive water splitting reaction; and (b) efficient charge separation/transfer to minimize recombination of electron-hole pairs.

1.1.1.2 Anostructure of semiconductors

The properties of nanomaterials could be very different from bulk materials, especially in semiconductor photocatalyst, size has been proved to play an important role for charges transfer and recombination in the photocatalytic hydrogen generation system.

1-D nanostructures are expected to have better charge transfer properties because of the shorter distance for recombination of charge carriers as well as advantageous charge transport along the axial direction [5-7]. 1-D TiO_2 nanostructures have been widely investigated as catalysts in photocatalytic systems or in photovoltaic devices. For example, Ramos-Sanchez et al. reported the hydrogen evolution using organic molecules functionalized Zn_3P_2 combined with the theoretical analysis [8]. They found the organic functional groups not only prevented Zn_3P_2 nanowire from degradation, but also improved the electron transfer from interior to the surface of nanowire. Cho et al. studied different nanowires-based photo-anode for PEC cell including TiO_2, α-Fe_2O_3, ZnO, and $BiVO_4$ [9]. The TiO_2 nanowire photo-anode showed the highest photocurrent density among the investigated samples. After a rapid flame treatment, the photocurrent increased by 2.7 times. Wang et al. used hydrogen treated TiO_2 (H:TiO_2) nanowires for PEC water splitting [10]. The pristine TiO_2 nanowires only showed 0.24% solar-to-hydrogen (STH) efficiency while H:TiO_2 showed a significant improvement to 1.63%. Other 1-D nanostructures, such as nanotube, nanoribbon, and nanorod also have been studied [11-13]. Zhang et al. designed an Au/TiO_2 nanotube photoelectrode and produced a photocurrent density of $\sim$150 $\mu A\ cm^{-2}$ [11]. Kiatkittipong et al. studied photocatalytic activity of sodium titanate ($Na_{1.48}H_{0.52}Ti_3O_7$), sodium hexatitanate ($Na_2Ti_6O_{13}$), andhydrogen titanate ($H_2Ti_3O_7$)

nanoribbons. They found the hydrogen evolution rate of $Na_2Ti_6O_{13}$ was 10 times higher than TiO_2 nanorods owing to the tunnel structure beneficial for separation of electrons and holes [12]. Takata et al. fabricated vertically aligned Ta_3N_5 nanorod for photoeletrochemical water splitting. A photocurrent density was improved by 3.2 times compared to that of a thin film electrode [13]. Therefore, recent studies indicate that 1-D nanomaterials are one of desired nanostructure for photocatalytic hydrogen evolution. In the dissertation, two types of 1-D nanomaterials, CuO/TiO_2 and Zn_3P_2 were evaluated for photocatalytic hydrogen production.

1.1.2 The use of microfluidic device and colloidal nanomaterial for study of enhanced oil recovery

Fossil fuel plays a very important role in our daily life. Oil and natural gas that are formed in the rock exists in the pore space during the rock formations. In the first stage of oil production, usually called primary production, the crude oil was coming through production well with assistance of nature pressure from the earth. Up to 20 % of crude oil could be recovered at this stage. Water injection is the strategy that often used to maintain reservoir pressure and to keep producing oil in the next step. This is so called secondary production and 15% to 20% of original oil in place is obtained. After primary and secondary production, at least 30-60% of original oil in place is still left in the oil field. Various physical and chemical methods are used for tertiary production, such as thermal, CO_2 injection, surfactant solution, polymer solution, and nanofluid. Tertiary production is also referred to enhanced oil recovery.

In a general laboratory evaluation of strategies of tertiary oil production, coreflood test is often used where a fluid or combination of fluids is injected into a sample of rock. Characteristics that affect rate of oil recovery, such as permeability, relative permeability saturation change, interaction between the fluid and the rock, are measured and evaluated. Meanwhile, geological conditions (temperature and pressure) could also be applied in coreflood test. The optimum formulation of fluids is determined based on the results of coreflood test and further evaluated for enhanced oil recovery in field. However, coreflood test is time-consuming and results are lack of microscopic point of view about how injected fluid interacted with rock. Microfluidic devices and "Lab on a chip" are emerging methods that have been applied as physical models of porous media for evaluating performance of tertiary oil production.

It is well-known that solid nanomaterials have been found to be capable of forming a densely packed layer at fluid-fluid interface, known as Pickering emulsion, to stabilize two immiscible liquids and to prevent destabilization by building up energy barriers at interface, which inspire many researchers to study the potential application in EOR. The type of formed emulsion droplets (water-in-oil or oil-in-water) is determined by the wettability of nanomaterials. The detachment energy required to remove adsorbed two dimensional nanodisks from the liquid-liquid interface can be described by the equation [14]:

$$\Delta G_{remove} = \pi R^2 \gamma_{oil-water} [1 - |1 - cos\theta|]$$

where R is the radius of nanoplatelets, γ is the interfacial tension between water and oil phase, and θ is the three phase contact angle. In addition, the emulsion droplets are also capable of withstanding harsh condition, such as high temperature and high pressure, without destabilizing during transport from reservoir to production well. In the dissertation, a commercial available microfluidic chip system and nanofluid containing colloid two dimensional nanodisks were used for obtaining preliminary results for study of EOR.

1.1.3 Synthesis Methods

Reflux and hydrothermal methods have been widely used for producing nanomaterials; however, relying on external heat transfer limit their applications. Microwave-assisted fabrication has received interests recently because it assists to reduce the reaction time significantly toward final products while quality are well-maintained. Microwave is defined as an electromagnetic energy with frequency ranging from 300 to 300000 MHz. Microwave-assisted heating is based on dipole rotation and ionic conduction. The former is that when reagents being irradiated by microwave, the dipoles existing in the molecules tend to align accordingly with the rapid oscillation of the applied electric field. Energies from the dielectric heating and friction of molecules are then released as heat. Therefore, homogeneous heating process of rapid temperature elevation is achieved by microwave dielectric heating. The latter is that free ionic species in reagents respond to the electric field. In the meantime, ionic motion is generated and rapidly alignment with electric field takes place that result in efficiently heating described previously. In comparison, conventional conductive heating methods (hydrothermal and

reflux), which depend on upon the inefficiently conductive heating by an external heat source. As a result, either extended reaction time or post treatment are required. In general, the reaction time for microwave-assisted fabrication of nanomaterials could be reduced dramatically from days to only hours with assistance of microwave heating.

Besides reagents, solvent also plays an important role in the synthesis since lots of reactions take place in solution and sometimes solvent is also involved in reaction. There are three main parameters, tangent delta (δ), dielectric constant (ε'), and dielectric loss (ε'') of a solvent that need to be considered in microwave-assisted synthesis. Tangent delta, defined as the ratio of dielectric loss to dielectric constant, which describes how efficiently microwave is converted to thermal energy. Dielectric constant of a solvent describes its ability to store electric charges and dielectric loss is describes the amount of input microwave energy that is dissipated as heat. Table 1 shows the parameters of some common solvents.

The frequency of microwave used in the dissertation is 2.45 GHz, which is equivalent to 1.0×10^{-5} eV, which is much lower than energy required to cleavage chemical bonds. Hence, microwave-assisted method is based on efficient heating rather than directly absorption of electromagnetic energy. In comparison, hydrothermal and reflux methods were also used for reference.

Parameters			
Solvent	Dielectric constant (ε')	Dielectric loss (ε'')	Tangent delta (δ)
Water	80.4	9.889	0.123
Ethylene Glycol	37	49.95	1.35
Methanol	32.6	21.483	0.659
Ethanol	24.3	22.866	0.941
DMF	37.7	6.07	0.161
Acetone	20.7	1.118	0.054

Table 1. Dielectric constant ($\boldsymbol{\varepsilon'}$), tan $\boldsymbol{\delta}$, and dielectric loss ($\boldsymbol{\varepsilon'}$) for 6 common solvent.

1.1.4 Outline of the Dissertation

The aim of this dissertation was originally motivated to synthesize nanomaterials using various nanotechnologies for different applications. Three different synthesis methods are used including hydrothermal, reflux, and microwave-assisted method. The applications mainly focus on photocatalytic hydrogen production and oil/water stabilization by amphiphilic nanodisks.

We demonstrated that microwave-assisted method can substantially reduce time for synthesis of nanomaterials. High temperature post-annealing are usually required to obtain anatase TiO_2. However, with assistance of microwave, anatase TiO_2 could be obtained in an hour at relative low temperature without post treatment. Similarly, ZrP nanodisks can also be obtained from microwave-assisted method requiring only an hour with well-controlled uniformity in polydispersity, size, aspect ratio, and shape.

This dissertation is organized as follows: In **Chapter II**, we investigate two types of one dimensional nanomaterials that are synthesized for photocatalytic hydrogen production. In **Chapter III**, we focus on different methods (hydrothermal, reflux, and microwave-assisted method) to synthesize two dimensional nanodisks for building-up a model system to study liquid crystal. In **Chapter IV**, we follow the microwave-assisted method developed in Chapter III to fabricate ZrP nanodisks and use it for Pickering emulsion stabilization. In **Chapter V**, new strategy to synthesize colloidal ZrP nanodisks are used for study of enhanced oil recovery (EOR) in a commercial microfluidic device. The synergic effect of combination of surfactant and colloidal ZrP nanodisks are also discussed. The result reveals the possibility of using nanomaterials for EOR to understand

the interaction between oil and nanomaterials. Finally, future work and ongoing projects are included in **Chapter IV**.

CHAPTER II

PHOTOCATALYTIC HYDROGEN PRODUCTION*

2.1 Synopsis

2.1.1 TiO_2 photocatalyst

As the first reported photocatalyst for water splitting under UV irradiation, TiO_2 has been extensively studied [2] because of low cost, good physical and chemical stability, and environmental compatibility. TiO_2 is reported to split water from water vapor, liquid water, and aqueous solutions containing electron donor [15-17]. The colloidal TiO_2 was found to efficiently generate H_2 under UV irradiation when combined with ultrafine Pt and RuO_2 particles [15]. The applications of TiO_2, however, are limited due to its large bandgap being responsive only to ultraviolet (UV)-light region. Prior research focused, therefore, on attempts to extend the absorption region of TiO_2 from UV to visible light by doping and formation of composites.

---

*Reprinted with permission from "Microwave-assisted synthesis of rod-like CuO/TiO_2 for high-efficiency photocatalytic hydrogen evolution" by Y.-H Yu, Y.-P Chen, Z. Cheng, 2015. International Journal of Hydrogen Energy, 40, 15994-16000, Copyright [2015] by Elsevier. Part of the data reported in this chapter is reprinted with permission from "Organic molecule-functionalized Zn_3P_2 nanowires for photochemical H_2 production: DFT and experimental analyses" by G. Ramos-Sanchez, M. Albornoz, Y.-H. Yu, Z. Cheng, V. Vasiraju, S. Vaddiraju, F. El Mellouhi, P.B. Balbuena, 2014. International Journal of Hydrogen Energy, 39, 19887-19898, Copyright [2014] by Elsevier.

2.1.2 Zn_3P_2 semiconductor

Zn_3P_2 is a good thermoelectric material to convert waste heat into electricity. Brockway et al. studies [18] reveal that Zn_3P_2 nanowires retained good thermoelectrical properties after manufacturing techniques, indicating its potential to be used used for energy application. Besides thermoelectric properties, the photoelectric properties of Zn_3P_2 has been studied since 1980s and was considered as a good candidate of material for solar cell [19].

2.2 Introduction

For energy generation, modern civilization relies largely upon fossil fuels, owing to their availability and developed infrastructures. Concerns over depletion and the effect of greenhouse gas emissions, however, have driven a shift in energy policy toward the development of clean and renewable energy. Hydrogen is a good candidate for energy application because of its high heat capacity compared to hydrocarbon fuels [20] and nearly zero greenhouse gas emissions.

2.2.1 TiO_2 photocatalyst

A variety of technologies has been applied to generate hydrogen energy and many strategies are considered [21-24]. Photocatalytic hydrogen evolution is considered to be a promising meaning of utilizing the sustainable natural resources of solar energy and water to generate hydrogen energy. In 1972, decomposition of water induced by the titanium dioxide (TiO_2) photoanode was developed by Honda and Fujishima [25]. Since then, research has focused on the study of various semiconductors for photocatalytic hydrogen evolution [26, 27]. Among semiconductors, TiO_2 has been widely investigated because it

is low cost, of good physical and chemical stability, mass-production, and environmental compatibility. Various morphologies of TiO_2, such as nanoparticles [28], nanotubes [29], and nanowires [10], have been extensively explored. The applications of TiO_2, however, are limited due to its large bandgap being responsive only to ultraviolet (UV)-light. Prior research focused, therefore, on attempts to extend the absorption region of TiO_2 from UV to visible light by doping [30, 31], noble metal deposition [32-34], and formation of composites [35], Previous studies also suggested that CuO/TiO_2 composites are good candidates for photocatalytic hydrogen evolution [36-38]. Although CuO/TiO_2 composites have been broadly studied, documentation of microwave-assisted synthesis in the literatures is still scarcely reported. Our research is intended to develop an efficient photocatalytic hydrogen evolution system from methanol-water aqueous solution by CuO-deposited TiO_2 rods, which are fabricated by a rapid and facile microwave-assisted process. Various effects, such as the quantity of photocatalyst used to produce hydrogen and the amount of CuO deposited onto TiO_2, were systematically investigated and evaluated.

2.2.2 Zn_3P_2 photocatalyst

Zn_3P_2 is a p-type semiconductor with a direct band gap in the range of 1.4-1.6 eV, which is ideal for solar energy conversion. More importantly, both elements, Zn and P, are abundant on earth, which can potentially reduce cost of photovoltaic modules based on Zn_3P_2. Bhushan and Catalano reported a solar cell with 5.96% energy conversion efficiencies based on poly-crystalline magnesium Zn_3P_2 diodes [39]. However, Zn_3P_2 is

very sensitive to oxygen and moisture that cause Zn_3P_2 degraded in ambient condition. This phenomenon can be described by the reaction below:

$$Zn_2P_2 + 6H_2O \rightarrow 3Zn(OH_2) + 2PH_3$$

$$Zn_2P_2 + 4O_2 \rightarrow 3Zn_3(PO_4)_2$$

Recently, Brockway et al developed an in-situ functionalization when growing Zn_3P_2 nanowires, which successfully protected the surface of nanowire and prevented from degradation [40]. Although Zn_3P_2 based solar cell has been developed, directly using Zn_3P_2 as photocatalyst to split water and produce hydrogen is scarcely reported in literatures. Hence, we want to further explore the possibilities to use Zn_3P_2 as an efficient photocatalyst.

2.3 Materials and Methods

2.3.1 Materials

All chemicals were of analytical grade and used as received without any further purification. Ethylene glycol ($C_2H_6O_2$), titanium butoxide ($C_{16}H_{36}O_4Ti$, TBT), titanium isopropoxide ($C_{12}H_{28}O_4Ti$, TTIP), and copper acetate ($Cu(CH_3COO)_2$) were purchased from Fisher Scientific Corp. (Pittsburgh, PA). Milli-Q water was used in all experiments.

2.3.2 Preparation of CuO/TiO_2 photocatalyst

Microwave-assisted fabrication has received interests recently because reaction time could significantly be reduced toward final products while quality of products are well-maintained. Conventional reflux and hydrothermal methods are often used to fabricate TiO_2 based materials in combination with the introduction of large quantities of

strong acids and bases for breaking, cleaning and recrystallizing TiO_2 crystals [41-43]. Both reflux and hydrothermal methods depend upon the inefficiently conductive heating by an external heat source, requiring either extended reaction time or post treatment to final products. In contrast, a homogeneous heating process of rapid temperature elevation is achieved by microwave dielectric heating [44]. As a result of being irradiated by microwave, the dipoles existing in the molecules tend to align accordingly with the rapid oscillation of the applied electric field. Energies from the dielectric heating and friction of molecules are then released as heat. In this study, the reaction time for fabricating rod-like TiO_2 is reduced dramatically from days to only a few hours with assistance of microwave heating.

Rod-like TiO_2 was synthesized by a facile two-step microwave-assisted solvothermal method without further calcination. In the first step, 1 mL of TBT was gradually added into EG in an 80 mL reaction vessel and dispersed by ultrasonication. The loaded vessel was then transferred to microwave oven (Discover SP, CEM Corp.) and heated at 170 °C for 20 minutes vigorous stirring. After the solvothermal process, the white titanium glycolate precipitates were obtained and collected by centrifugation, washed thoroughly by ethanol several times, and dried in an oven at 60°C under ambient conditions. In the second step, 0.4 g of titanium glycolate obtained in the first step was suspended in an 80 mL reaction vessel filled with 40 mL of water and then heated, microwave-assisted, at 150 °C for 30 min. The obtained white rod-like TiO_2 resultants were collected and washed following the same procedures of the first step. CuO/TiO_2 rod photocatalysts were prepared in a similar way of the first step. An appropriate quantity of

TiO_2 rod samples was suspended in the desired concentration of copper acetate aqueous solution and subjected to microwave-assisted heating at 150 °C for 30 minutes. Finally, the CuO/TiO_2 rod photocatalysts were washed several times by Milli-Q water to remove any possible impurities and dried in an oven at 60 °C overnight. The weight percentage of CuO deposited on TiO_2 rods were designed as 0, 0.5, 1, 5, 10 wt% CuO/TiO_2 and herein denoted as TR, CTR0.5, CTR1, CTR5, and CTR10, respectively. TiO_2 rods and CuO nanoparticles were synthesized and characterized separately for reference.

2.3.3 Preparation of Zn_3P_2 photocatalyst

The Zn_3P_2 sample used in the dissertation was synthesized by chemical vapor deposition (CVD) and kindly provided by Dr. Sreeram Vaddiraju's group. CVD has been used for fabricating thin-film as well as bulk material and powders. There are multiple steps involved in the growth of nanomaterials including transport of reactant species into the reactor, reaction in the substrate, and removal of reaction products. CVD is also capable of producing nanomaterial in large quantity, such as carbon nanotubes, graphene, Zn_3P_2 nanowires [45-47]. A three-zone hot-walled CVD chamber was used and the obtained Zn_3P_2 nanowires were in-situ functionalized by two types of organic molecules: 4-aminothiophenol (4-ATP) and 1,3 propanedithiol (1,3-PDT).

2.3.4 Characterization

The as-synthesized CuO/TiO_2 photocatalysts were grounded into fine powders for following characterization. X-ray powder diffraction was taken by a Bruker-AXS D8 Advanced Bragg–Brentano X-ray powder diffractometer using a graphite monochromator

with Cu k_α X-ray radiation operated at 40 kV and 40 mA under θ –2θ configuration. The morphologies were characterized by field emission scanning electron microscopy (FE-SEM, Quota 600) and high-resolution transmission electron microscopy (HR-TEM, JEOL 2010). Specific surface area was determined by nitrogen adsorption−desorption isotherms at 77 K by a physisorption analyzer (ASAP 2020, Micromeritics). UV-Vis spectra were performed with a UV-Vis-NIR spectrophotometer (U-4100, Hitachi).

2.3.5 Photocatalytic hydrogen evolution

Photocatalytic hydrogen evolution was carried out in a 250 mL Pyrex water-jacketed round bottom flask. First, CuO/TiO_2 rods were introduced into 150 mL of methanol-Milli-Q water aqueous solution (20%/80% V/V) and mixed vigorously by a magnetic stirring bar. The system was degassed 30 minutes prior to irradiation by ultrasonication and N_2 gas was used to remove any oxygen in the system. The photocatalytic system was irradiated with a 300-watt xenon lamp (PE300BF, Cermax) at a distance of 20 cm. Temperature of photocatalytic system was controlled at 25°C by circulating cooling water in all experiments. The amount of produced hydrogen was monitored, extracted by a gas-tight syringe, and analyzed at 30-minute intervals by gas chromatography (GC, Agilent 7820A) with a thermal conductivity detector equipped with a 5-Å molecular sieve column. The experimental setup is shown in Figure 2.

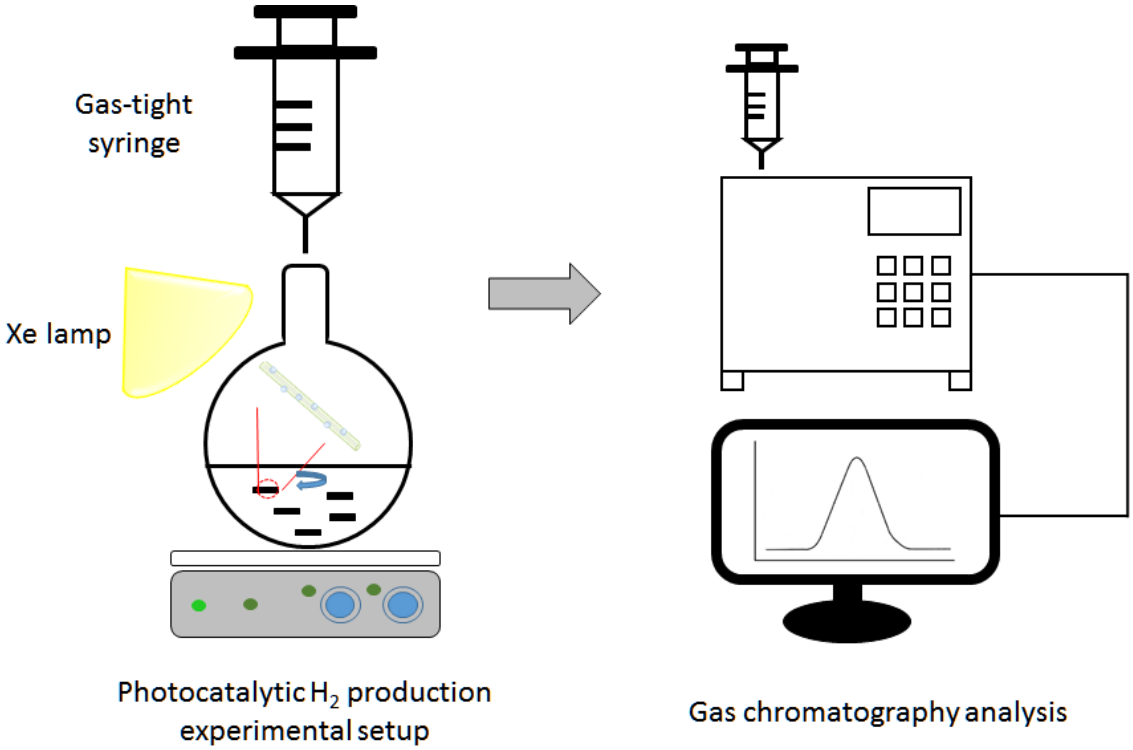

Figure 2. Photocatalytis H_2 production experimental setup

2.4 Results and Discussion

2.4.1 CuO/TiO₂ photocatalyst

XRD patterns of the obtained CuO/TiO_2 photocatalysts with different deposited weight percentage of CuO are shown in Figure 3. As-prepared pure TiO_2 shows the typical diffraction peak (101) of anatase TiO_2 along with other peaks of (004), (200), (105), (204), etc. The broadening peaks indicate the nanocrystalline nature of TiO_2. At loading concentration below 5 wt%, the diffraction peaks of CuO are barely seen, which can be attributed to CuO crystals were well-dispersed in TiO_2 rods [48]. While at higher loading concentration (> 5 wt%), the diffraction peaks show highly-crystallized CuO/TiO_2

composites. The Scherrer equation was employed to calculate the average crystalline size of TiO_2 samples:

$$d = k\lambda/\beta\cos\theta$$

where d is the average crystallite size; λ is the X-ray wavelength (1.5418 Å for Cu K_α); k is a constant (0.89); β is the full-width at half-maximum for the peak at 2θ = 25.33°; and θ is the angle of the diffraction peak. The calculated average crystalline size of TiO_2 is 9 nm based on diffraction peak (101) of anatase TiO_2.

Further, the morphologies of CuO/TiO_2 photocatalytsts were observed by FE-SEM and HR-TEM, as shown in Figure 4. Figure 4a exhibits the representative as-prepared TiO_2 products with rod-like shape and the dimensions are tens of micrometers in length and 0.5 to 3 μm in diameter. It can be observed that some longer rods broke into several shorter segments of rod as a result of sample preparation. Individual TiO_2 rods (Figure 4b) show uniform rectangular-like cross-sections. Some rod-like TiO_2 with large diameters can be found in Figure 4a inset that could be ascribed to a bundle of small rectangular rods forming a large rod.

Figure 4(c-d) present TEM images of TiO_2 rod. It is clear that a TiO_2 rod consists of numerous interconnected TiO_2 nanoparticles with diameter less than 10 nm (Figure 4c). The selected area electron diffraction (SAED) pattern shows a spotty ring indicating the characteristic of polycrystalline which is consistent with the result of XRD analysis. Figure 4d presents an HR-TEM image of a TiO_2 rod. The spacing between lattice fringes is 0.35 nm and can be indexed to the plane (101) of anatase TiO_2.

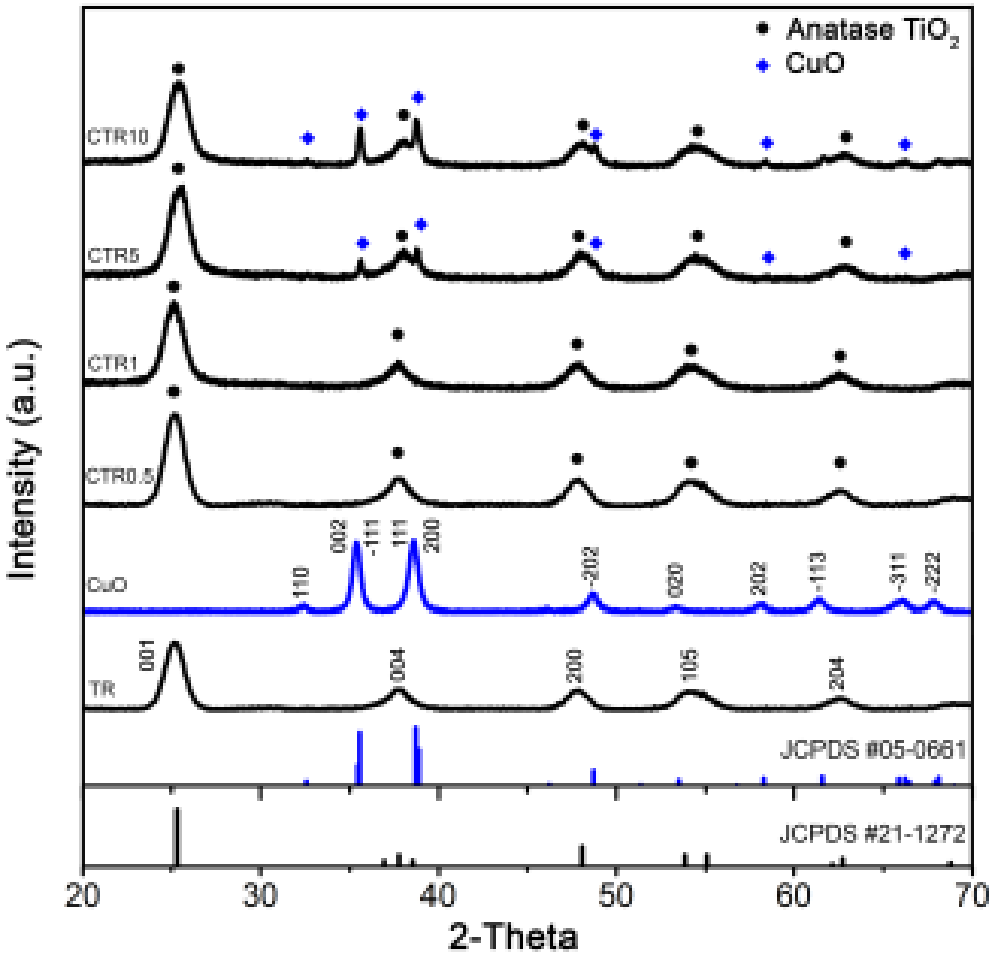

Figure 3. X-ray diffraction spectra of microwave-assisted synthesized photocatalysts. (from top) CTR10, CTR5, CTR1, CTR0.5, CuO, and TR.

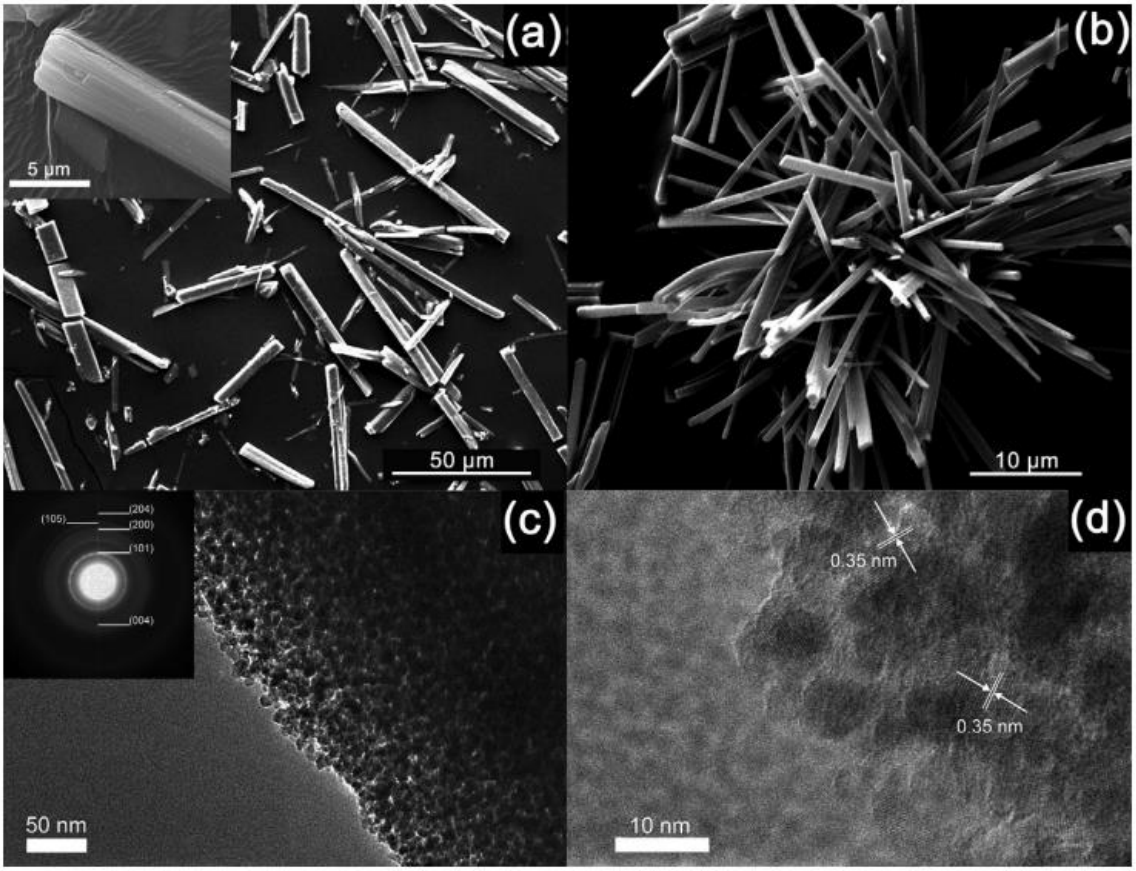

Figure 4. The SEM images of (a) TR, (b) TR at higher magnification, and TEM images of (c) porous TR (SAED, inset), and (d) lattice fringes of TR in HR-TEM.

In the preliminary test, time dependence of photocatalytic hydrogen evolution from TiO_2 rods with various CuO content under light irradiation are displayed in Figure 5. Pure TiO_2 rods were adapted for the control experiment. It could be observed that the hydrogen evolution rates increased after deposition of CuO. Without CuO deposition, the photocatalytic hydrogen evolution rate of TiO_2 rods was as low as 45.4 μmol g^{-1} h^{-1}. Using CTR0.5, the photocatalytic hydrogen evaluation showed a slightly improved hydrogen evolution rate of about 3.5-fold of pure TiO_2 rods. With 1 wt% CuO deposition, the photocatalytic activity was greatly enhanced and the hydrogen evolution rate reached as

high as 3508.7 ± 97 μmol g^{-1} h^{-1}, which is about 77-fold of that of bare TiO_2 rods. At higher loading of CuO over 1 wt%; however, the hydrogen evolution rate was inversely proportional to the loading amount of CuO. This phenomenon could be explained by two mechanisms. First, the size of CuO nanoparticles is much larger than that of a single TiO_2 particle, as shown in Figure 6. Consequently, higher CuO content-decorated TiO_2 results in the decrease in surface area of bulk material, suggesting the active sites for water-splitting was decreased as well. Second, it was confirmed by Bandara *et al*. that larger amount of CuO-loaded TiO_2 leads to migration of CB toward less negative position [49].

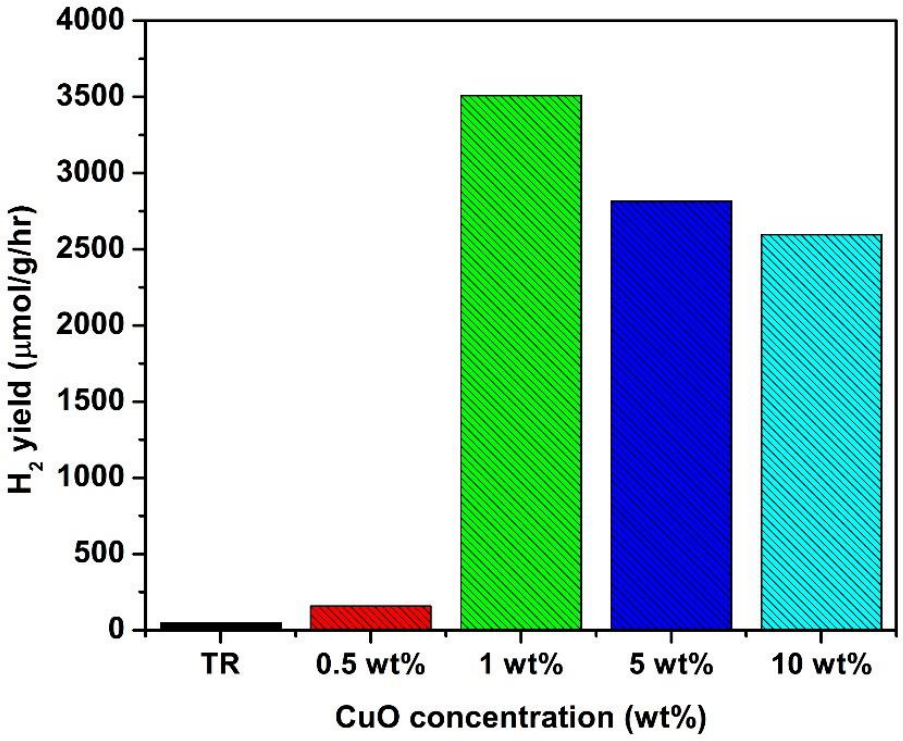

Figure 5. The dependence of CuO concentration on the photocatalytic activity of resultant CuO/TiO_2 photocatalysts for hydrogen evolution.

The shift of CB position results in the decrease in potential of photogenerated electrons and a decrease in photocatalytic activity. The results suggest that an appropriate amount of CuO deposition would be necessary for enhancing light harvesting and photocatalytic activities.

The DR-UV-Vis spectra of the CuO deposited TiO_2 photocatalysts as well as pure TiO_2 are depicted in Figure 7. The spectrum of TiO_2 shows an absorption edge at 388 nm in the UV-region, while spectra of CuO deposited TiO_2 show a two-phase adsorption in the UV as well as in the visible light region. This behavior could be ascribed to that the composites were formed of two types of materials corresponding to TiO_2 and CuO compounds. The broad band between 400-800 nm implies a significant improvement of absorption in the visible light region. It can be seen that the adsorption edge of all prepared samples did not shift, which indicates that CuO were deposited onto TiO_2 rods surface rather than doped into the TiO_2 crystalline. The enhanced light adsorption increased the possibilities to separate electrons and holes; thus, the photocatalytic H_2 evolution was improved as well.

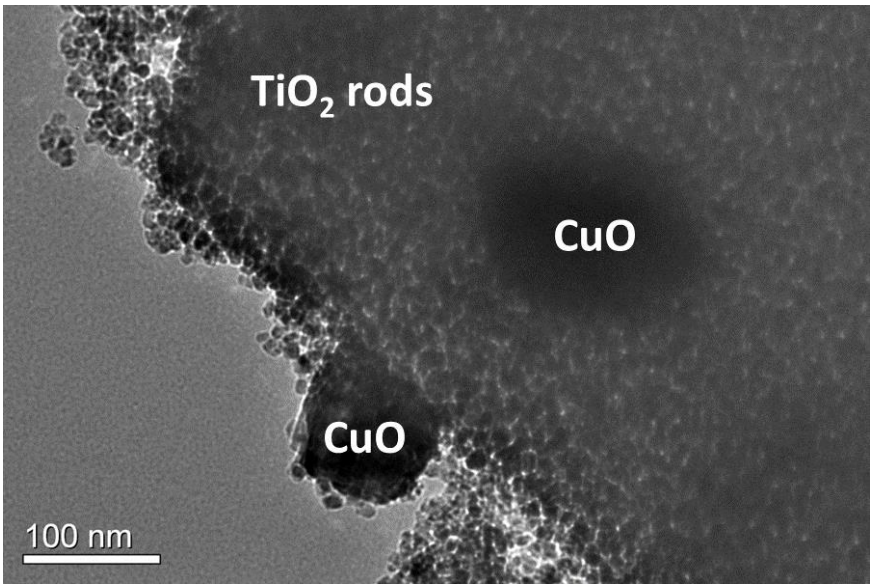

Figure 6. TEM image of CTR1

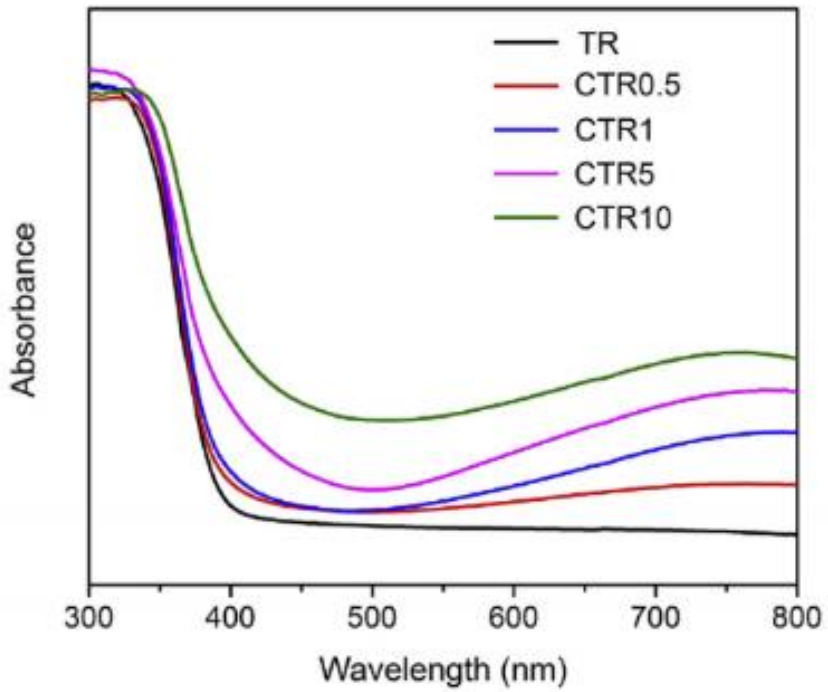

Figure 7. DR-UV-Vis spectra of the photocatalysts TR, CTR0.5, CTR1, CTR5, and CTR10.

In order to realize the effect of deposition of CuO nanoparticles on microstructure of the formed composite, nitrogen adsorption-desorption isotherm was used to analyze the porous structure and the result was depicted in Figure 8. The isotherm shows a typical multi-layer adsorption behavior and demonstrates the porous nature of synthesized CuO/TiO_2 rods. The specific surface area of TiO_2 rods was 269.6 m^2/g obtained from Brunauer−Emmett−Teller (BET) adsorption isotherms analysis. Although a slightly decrease from 269.6 to 249.1 m^2/g in specific surface area after deposition of 1wt% of CuO was observed, the average pore size and distribution (Figure 8 inset) of both products were about the same (10-12 nm), indicating deposited CuO nanoparticles only had a minor impact on the microstructure of TiO_2 rods. Compared to specific surface area of commercial P25 TiO_2 nanoparticles (ca. 50 m^2/g), the CuO/TiO_2 photocatalysts are able to provide with significantly increased surface area for photocatalytic hydrogen evolution taking place.

Since CTR1 shows the best photocatalytic performance among all investigated photocatalysts, it was selected for determination of optimum amount and durability test. Various amount of CTR1 were used to perform photocatalytic hydrogen evolution; the results are plotted in Figure 9. It has been observed that produced hydrogen increased with time linearly, implying reliable photocatalytic activity and stability. It is also noted that the hydrogen evolution rate was reduced with increasing amounts of photocatalyst in150 mL of methanol-Milli-Q water aqueous solution, as shown in Figure 10. This reduction might be due to the fact that an increased amount of photocatalyst shadows the existing photoelectric reactions, suggesting that use of appropriate amount of photocatalyst would

be beneficial for photocatalytic hydrogen evolution. In a 4-hour test period, the use of 30 mg CTR1 photocatalyst performed the highest hydrogen evolution, a rate as high as 3508.7 ± 97 μmol h^{-1} g^{-1}. The solutions of 50 mg and 100 mg CTR1 photocatalyst showed the hydrogen evolution rates of 2967 ± 155 μmol h^{-1} g^{-1} and 1720 ± 37 μmol h^{-1} g^{-1}, respectively. A solution of 0.2 g/L was determined, therefore, to be the optimum ratio of photocatalyst and aqueous solution in the following photocatalytic hydrogen evolution tests.

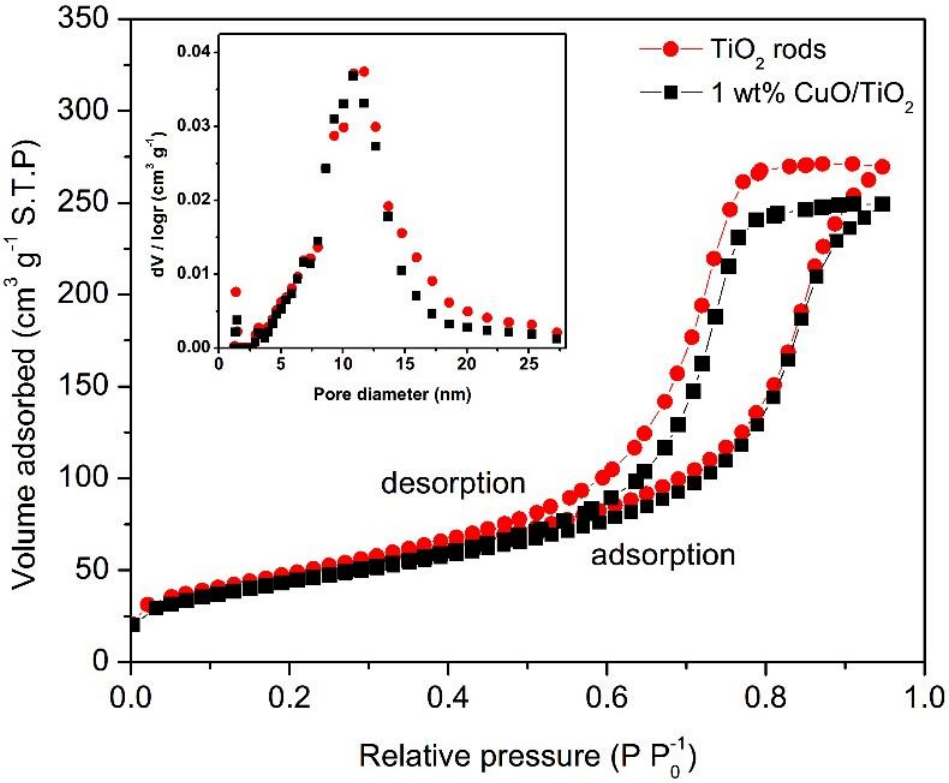

Figure 8. Nitrogen adsorption-desorption isotherms of the TR and CTR1 photocatalyst and pore size distribution calculated from the desorption isotherm using the Barrette-Joynere-Halenda (BJH) analysis method (inset).

In order to perform the reproducibility test, CTR1 was examined continuously (Figure 11). The photocatalytic hydrogen evolution was carried out for five cycles without replacing photocatalysts and methanol-Milli-Q aqueous solution. The system was purged with N_2 gas every 4 hours to remove hydrogen produced in previous cycle. Neither a decrease in hydrogen evolution rate nor obvious deactivation of the photocatalyst was noticed. Some studies indicated a slow starting hydrogen evolution rate might be observed in the beginning, and a stabilizing time is needed for the photocatalyst to reach its best performance [27, 50]. However, the phenomenon was not observed in this study, suggesting that surface characteristics of our photocatalysts are stable and ready to be used right after synthesis.

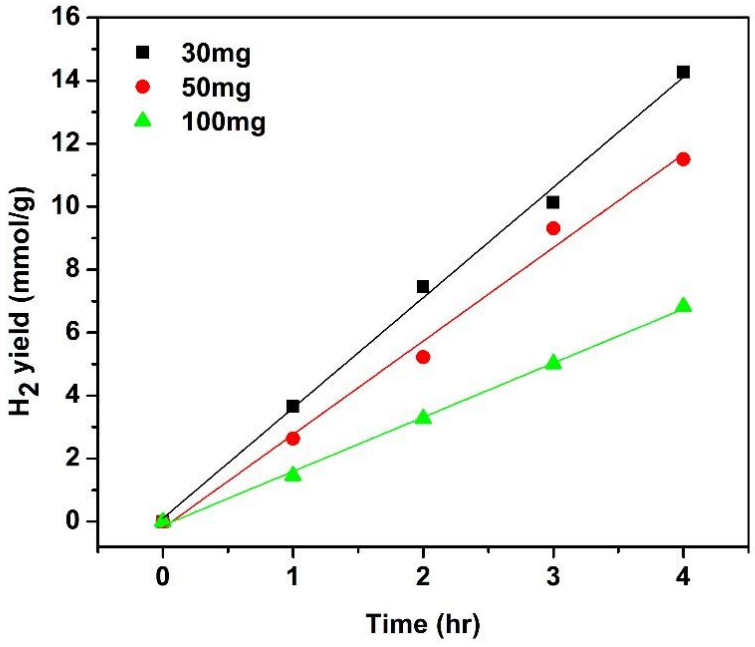

Figure 9. Photocatalytic hydrogen evolution results of using different amounts of CTR1 photocatalysts suspended in 150 mL methanol-Milli-Q aqueous solution.

The possible mechanism of photocatalytic hydrogen evolution is shown in Figure 12. It was reported that overall water splitting without assistance of sacrificial agent is unlikely due to fast combination of electron-hole pairs and backward reaction [51]. Thus, using solely TiO_2 or CuO to produce hydrogen photocatalytically would be inefficient. The bandgap diagram of the CuO/TiO_2 junction provides a better configuration for light harvesting. As shown in Figure 12, the CB of TiO_2 is more negative than that of CuO, which means photogenerated electrons in CB of TiO_2 will migrate and accumulate in the CB of CuO. Hence, the resulting band configuration would be more favorable for reducing water to hydrogen [49], combining the benefits of the UV-response from TiO_2 and the more positive CV position of CuO. The migration of photogenerated electrons of TiO_2 will help to improve separation of electron-hole pairs. As a result, the efficiency of photocatalytic hydrogen evolution will increase.

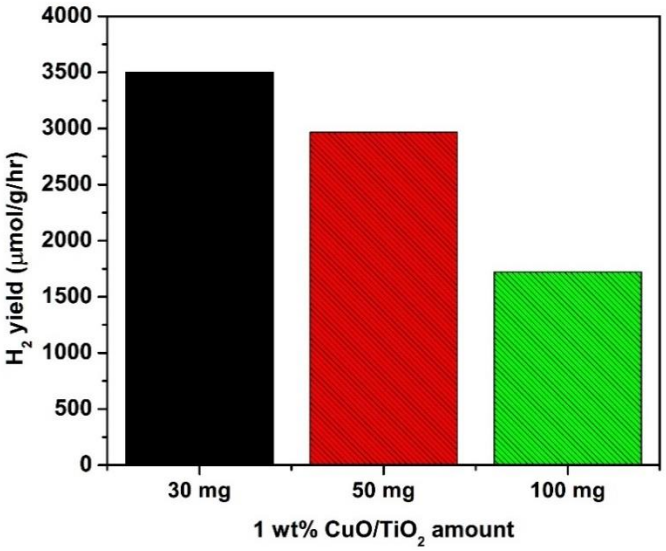

Figure 10. Photocatalytic hydrogen evolution results of the dependence of CTR1 amount on photocatalytic activity for hydrogen evolution.

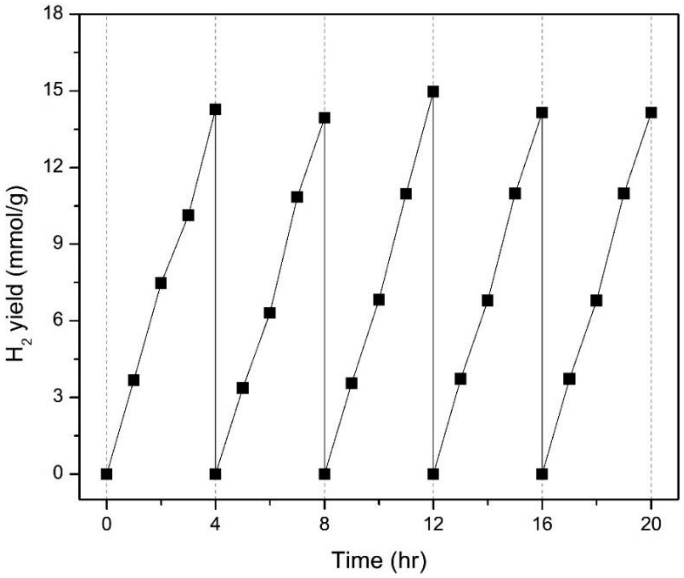

Figure 11. Reproducibility test of hydrogen evolution of CTR1.

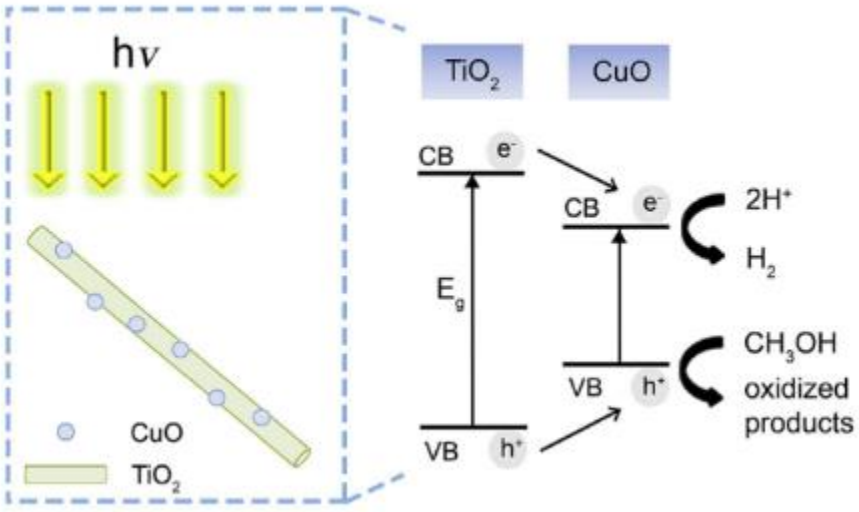

Figure 12. Schematic illustration of energy band diagram of CuO/TiO_2 for photocatalytic hydrogen evolution. CB: conduction band and VB: valence band.

2.4.2 Zn_3P_2 photocatalyst

Figure 13 shows the FESEM images of Zn_3P_2 nanowires functionalized with different functional groups before (a-c) and after (d-f) photocatalytic hydrogen production. Figure 13a indicates as-synthesized Zn_3P_2 nanowires are 50-100 nm in diameter and tens of μm in length. It can be found in Figure 13b and 14c that morphologies of Zn_3P_2 nanowires were still kept after *in situ* functionalization. However, the morphologies of Zn_3P_2 transformed from nanowires to small pieces or shorter wires after photocatalytic hydrogen production except for Zn_3P_2-PDT (Figure 13f). The transformation of morphologies could be the result from Zn_3P_2 reacting with water and forming zinc hydroxide, which can be suggested as below [40].

$$Zn_3P_2 + 6H_2O \rightarrow 3Zn(OH)_2 + 2PH_3 \quad \text{eqn 2.1}$$

Zn_3P_2 based materials have been studied as solar cell [52, 53], however, to the best of our knowledge, it is the first time that hydrogen production was performed photocatalytically over Zn_3P_2 nanowires. Photocatalytic hydrogen production activity over Zn_3P_2 nanowires was carried out in aqueous solution containing 20 vol% of methanol acting as a hole scavenger. Figure 14 displays time courses of photocatalytic hydrogen production from different Zn_3P_2 nanowires under visible light irradiation. In this work, pristine Zn_3P_2 nanowires and functionalized Zn_3P_2 nanowires with 4-ATP and 1, 3 PDT molecules were tested. The results indicate that hydrogen production rates over pristine Zn_3P_2 Zn_3P_2-ATP, and Zn_3P_2-PDT are 0.03 ± 0.001, 6.52 ± 0.36, and 12.15 ± 0.34 mmol h^{-1} g^{-1}, respectively.

Gentle amount of produced hydrogen was observed in the first half hour presented in all tests. It could be explained as all Zn_3P_2 nanowires were undergoing the photochemical activation process [50] and further increasing evolved hydrogen with increasing time. In addition, after 4 hr of irradiation, only negligible amount of hydrogen was produced by pristine Zn_3P_2. This could be ascribed to the fact that pristine Zn_3P_2 reacts easier with water forming zinc hydroxide more rapidly than the other two functionalized nanowires, which is in consistent with **eqn (2.1)** and FESEM image (Figure 13d). Zn_3P_2-ATP showed enhanced hydrogen production that is 217 times higher than pristine Zn_3P_2 nanowires. Among the investigated samples, Zn_3P_2-PDT presents the highest hydrogen evolution rate that evolved hydrogen 405 times and nearly twice higher than that of pristine Zn_3P_2 and Zn_3P_2-ATP, respectively. It could be attributed to a better protection exerted by this molecular system that prevents nanowire degradation and formation of Zn hydroxide, in agreement with the FESEM image (Figure 13f) illustrating that Zn_3P_2-PDT kept its morphology in spite of the oxidation environment. Functionalized Zn_3P_2 nanowires reveal comparable hydrogen production rate to reported benchmarking visible-light responsive semiconductors [54-56] and shows the potential to keep developing this photoelectrochemical system by using earth-abundant elements.

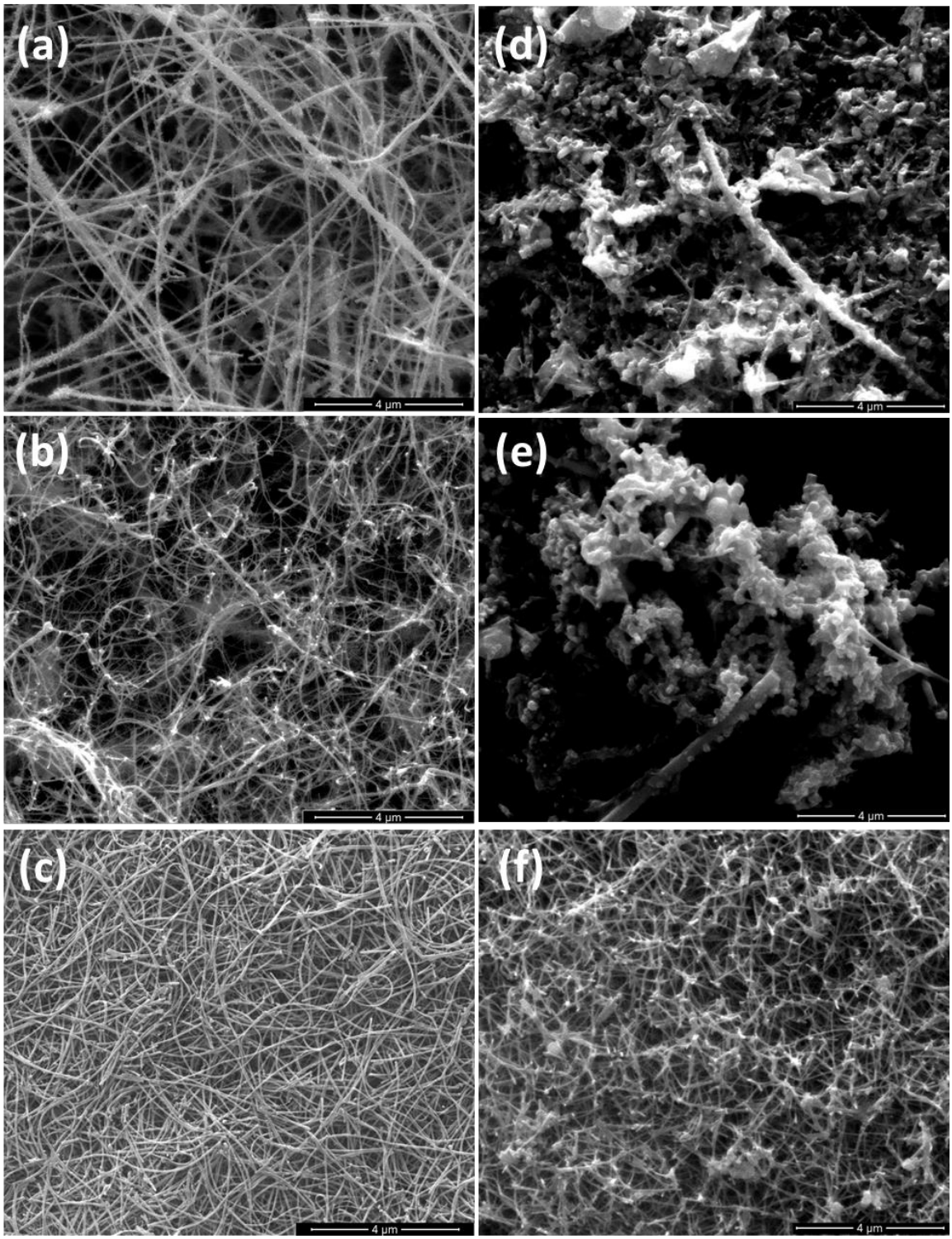

Figure 13. FE-SEM images of unfunctionalized Zn_3P_2, Zn_3P_2-ATP, and Zn_3P_2-PDT nanowires before (a-c) and after photocatalytic hydrogen production (d-f), respectively.

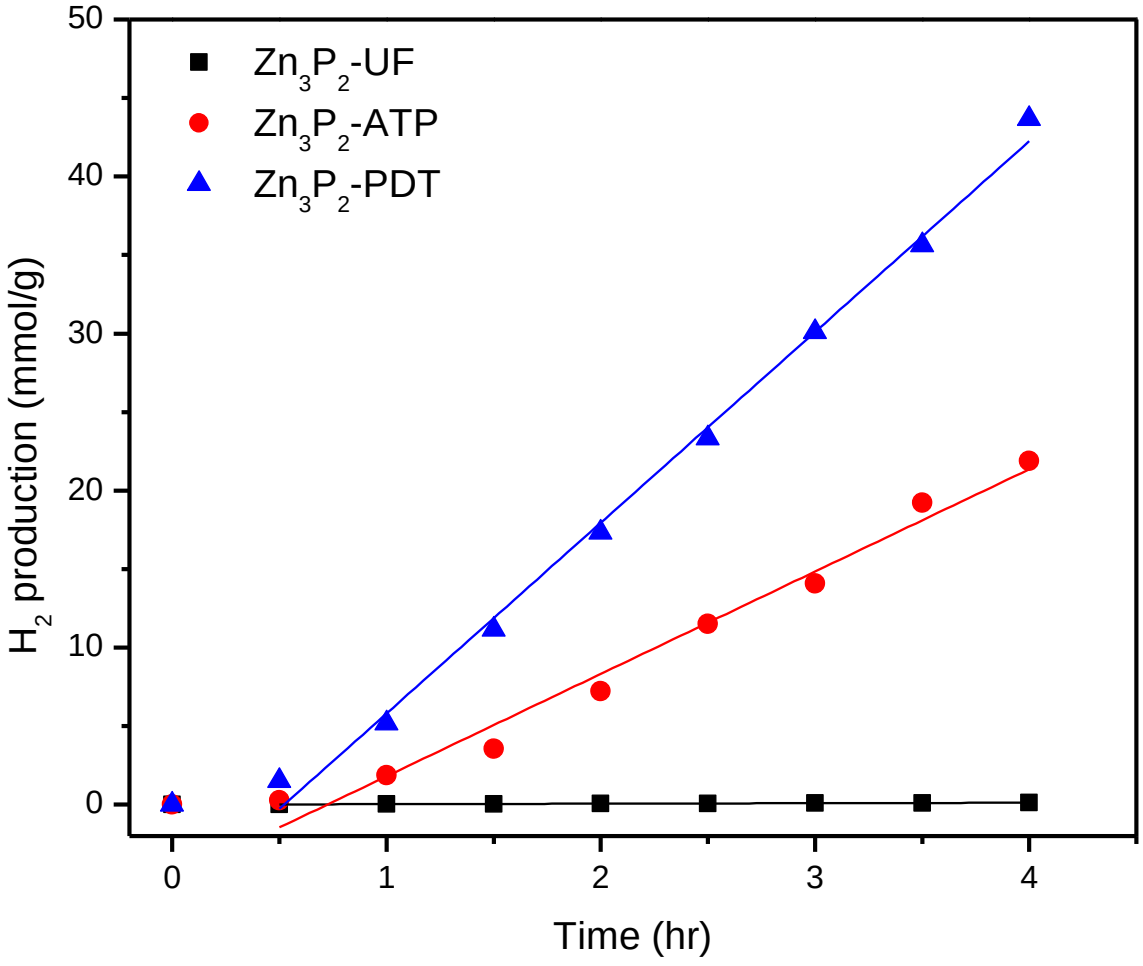

Figure 14. H_2 production (in mmol/gr) for Zn_3P_2 nanowires unfunctionalized (black squares), ATP-coated (red circles), and PDT-coated (blue triangles).

2.5 Conclusion

Two one dimensional nanomaterials, CuO/TiO_2 and Zn_3P_2, were evaluated for efficient photocatalytic hydrogen production. A green, easy, and fast microwave-assisted solvothermal method to fabricate CuO decorated TiO_2 rods for efficient photocatalytic hydrogen evolution was established. The decoration of CuO not only improved the adsorption of light energy, but also enhanced the charge separation; as a result, highly

efficient hydrogen evolution was accomplished. 1 wt% of CuO deposited TiO_2 rods were found to exhibit the best performance of photocatalytic activity and stability for water splitting. A specific hydrogen evolution rate as high as 3508.7 μmol g^{-1} h^{-1} was achieved with the present product. In addition, experiments show that Zn_3P_2 coated with 1,3-PDT molecules depict better resistance to degradation than coating using 4-ATP molecules, hence providing a superior H_2 yield. Zn_3P_2 nanowires functionalized with 4-ATP and 1,3-PDT molecules greatly enhanced hydrogen evolution rates by 217 and 405 times higher than that of non-functionalized Zn_3P_2 nanowires, respectively.

CHAPTER III

FABRICATION OF NANODISKS*

3.1 Synopsis

Due to their abundance in natural clay and potential applications in advanced materials, discotic nanoparticles are of interest to scientists and engineers. Growth of such anisotropic nanocrystals through a simple chemical method is a challenging task. In this study, we fabricate discotic nanodisks of zirconium phosphate [$Zr(HPO_4)_2 \cdot H_2O$] as a model material using hydrothermal, reflux and microwave-assisted methods. Growth of crystals is controlled by duration time, temperature, and concentration of reacting species. The novelty of the adopted methods is that discotic crystals of size ranging from hundred nanometers to few micrometers can be obtained while keeping the polydispersity well within control. The layered discotic crystals are converted to monolayers by exfoliation with tetra-(n)-butyl ammonium hydroxide [$(C_4H_9)_4NOH$, TBAOH]. Exfoliated disks show isotropic and nematic liquid crystal phases. Size and polydispersity of disk suspensions is highly important in deciding their phase behavior.

---

*Reprinted with permission from "Synthesis and exfoliation of discotic zirconium phosphate to obtain colloidal liquid crystals" by Y.-H Yu, X. Wang, A. Shinde, Z. Cheng, 2016. Journal of Visualized Experiments, 111, e53511, Copyright [2016] by MYJoVE Corporation.

3.2 Introduction

Discotic colloids are naturally abundant in the form of clay, asphaltene, red blood cells, and nacre. A range of applications in many engineered systems, including polymer nanocomposites [57], biomimetic materials, functional membranes [58], discotic liquid crystal studies [59] and Pickering emulsion stabilizers [60] are developed based on discotic colloidal nanodisks. Nanodisks with uniformity and low polydispersity is important for studying phases and transformations of liquid crystals. Zirconium phosphate (ZrP) is a synthetic nanodisks with well-ordered layered structure and controllable aspect ratio (thickness over diameter). Therefore, the exploration of different synthesis of ZrP helps to establish fundamental understanding of discotic liquid crystal system.

The structure of ZrP was elucidated by Clearfield and Stynes in 1964 [61]. For the synthesis of layered crystals of ZrP, hydrothermal and reflux methods are commonly adopted [62, 63]. Hydrothermal method gives a good control on size ranging from 400 to 1500 nm and polydispersity within 25% [62], while reflux method gives smaller crystals for the same duration time. Microwave heating has been proven to be a promising method for synthesis of nanomaterials [64]. However, there are no papers describing synthesis of ZrP based on microwave-assisted route. The effective control over size, aspect ratio, and mechanism of the crystal growth by hydrothermal method was systematically studied by our group [62].

ZrP can be easily exfoliated into monolayers in aqueous suspensions, and the exfoliated ZrP have been well established as liquid crystal materials in Cheng's group [59, 65-69]. So far, exfoliated ZrP nanodisks with various diameters, say different aspect ratios,

have been studied to conclude that larger ZrP had the I (isotropic)-N (nematic) transition at lower concentration compared to smaller ZrP [59]. The polydispersity [59], salt [65] and temperature [66, 67] effects on the formation of nematic liquid crystal phase have been also considered. Moreover, other phases, such as sematic liquid crystal phase, have been investigated as well [67, 69].

In this chapter, we demonstrate experimental realization of such a colloidal ZrP nanodisks suspension. Layered ZrP crystals are synthesized via different methods, and then are exfoliated in aqueous media to obtain monolayer nanodisks. At the end, we show liquid crystal phase transitions exhibited by this system. A notable aspect of these disks is their highly anisotropic nature that the thickness to diameter ratio is in the range of 0.0007 to 0.05 depending on the size of disks [59]. The highly anisotropic monolayer nanodisks establish a model system to study phase transitions in the suspensions of nanodisks.

3.3 Materials and Methods

3.3.1 Synthesis of α-ZrP using hydrothermal method

4 g of zirconyl chloride octahydrate ($ZrOCl_2 \cdot 8H_2O$) was dissolved in 2.5 mL deionized (DI) water in a 150 mL round bottom flask. 37.5 mL of 12 M phosphoric acid (H_3PO_4) was dropwise introduced into the $ZrOCl_2$ solution under vigorous stirring. The resulting gel-like mixture was poured into Teflon-lined pressure vessel of 80 mL volume, then the vessel was placed into hydrothermal autoclave composed of stainless steel shell and lid, pressure plate and was heated in convection oven at 200 °C for 24 hours. When the reaction was finished, the hydrothermal autoclave was cool down 8 hours to room temperature under ambient cooling. ZrP nanodisks was collected in centrifuge and washed

with water several times until the acid was washed away. The resulting ZrP slurry was dried in oven at 65 °C for 8 hours and then grind it using a pestle and mortar.

3.3.2 Synthesis of α-ZrP by reflux method

6 g of $ZrOCl_2 \cdot 8H_2O$ was mixed with 50 mL of 12 M phosphate acid in a 150 mL round bottom flask. Then the mixture was reflux in an oil bath with a condenser at 94 °C for 24 hours. The resultant was cleaned and collected in the same manner mentioned in 3.4.1. The product was with DI water three times and then dried in the oven at 65 °C for 8 hours. The dried bulky ZrP sample was grinded into powder using a pestle and mortar, and stock for later use.

3.3.3 Synthesis of α-ZrP by microwave-assisted method

The microwave-assisted synthesis was beginning with mixture of 1 g of $ZrOCl_2 \cdot 8H_2O$ into 9 mL of 12 M phosphoric acid solution, and stir the resulting mixture well in a 20 mL scintillation vial. Then 5 mL of the above mixture was poured into a 10 mL glass vessel specified for microwave reactor. The reaction temperature was set at 150 °C, pressure limit at 200 psi and allow the reaction to happen for 1 hour. After the reaction, let the glass vessel cool down for about 15 min and then follow the same procedure as in 3.4.1 and 3.4.2 for acid washing and drying of α-ZrP crystals.

3.3.4 Exfoliation of layered α-ZrP into monolayers

1 g of α-ZrP was suspended into 10 mL of DI water in a 20 mL scintillation vial. 2.2 mL of TBAOH (40 wt. %) was introduced into it and vortex for at least 40 sec. Notice that molar ratio of Zr:TBAOH is kept as 1:1. After, the resulting concentrated suspension was sonicated for 1-2 hours and leave for 3 days to allow full intercalation of TBA^+ ions

and complete exfoliation of crystals. Optionally, concentrated suspension can be diluted (2 to 3 times dilution) with water to obtain better exfoliation. Finally, the exfoliated samples was centrifuged at high rotation speed to remove partially exfoliated crystals settled at the bottom. The top part (exfoliated ZrP) was collected in another container, and the procedure was repeated until no sediment is found.

3.4 Results and Discussion

Figure 15-18 show SEM images of α-ZrP nanodisks obtained from hydrothermal, reflux, and microwave-assisted methods, respectively. It was observed that α-ZrP nanodisks show hexagonal in shape and different thickness depending on synthesis conditions and prepared methods. A previously reported study from our group [62] suggests that for the crystal growth time 48 hours or above, the edge of the disks become sharper. Usually, the reflux method yields nanodisks smaller in size and less regularly hexagonal in shape than the α-ZrP obtained by hydrothermal method at similar reaction conditions including concentration of phosphoric acid and reaction time [62, 63].

Figure 18 shows dynamic light scattering (DLS) result of the size distribution of exfoliated ZrP suspensions by three different synthesize methods accordingly. The reflux method is a good option for making a smaller size of α-ZrP with a uniform diameter and thickness. Similar to the hydrothermal method, the reflux method is limited by the preparation time. In general, it takes longer time for the crystals to grow. The longer reaction time required for reflux method may result in nanodisks with a larger size. The average size of exfoliated nanodisks is measured by DLS. In this study, the size of exfoliated ZrP nanodisks is 1021.5 nm with 19.6% polydispersity, 289.8nm with 7.0%

polydispersity, and 477.5 nm with 19.1% polydispersity for hydrothermal method (12 M H_3PO_4, 24 h), reflux method (12 M H_3PO_4, 24 h) and microwave-assisted synthesis (15 M H_3PO_4, 1 h) respectively. We also have found that the reflux method can be used to synthesize a different phase of ZrP, theta-ZrP (θ-ZrP) which has larger interlayer spacing compared to α-ZrP, by changing the mixture procedure and the concentration of the materials. For example, θ-ZrP disks with a mean size of 120 nm and thickness of 12 nm were prepared via the reflux method starting with drop-wise addition of 35 wt% H_3PO_4 into a diluted solution of $ZrOCl_2$ [70]. In order to obtain uniform α-ZrP nanodisks, the most critical step in the synthesis procedure is to ensure that all of the precursors are well mixed. When phosphoric acid is introduced into $ZrOCl_2$ solution, the gel will be quickly

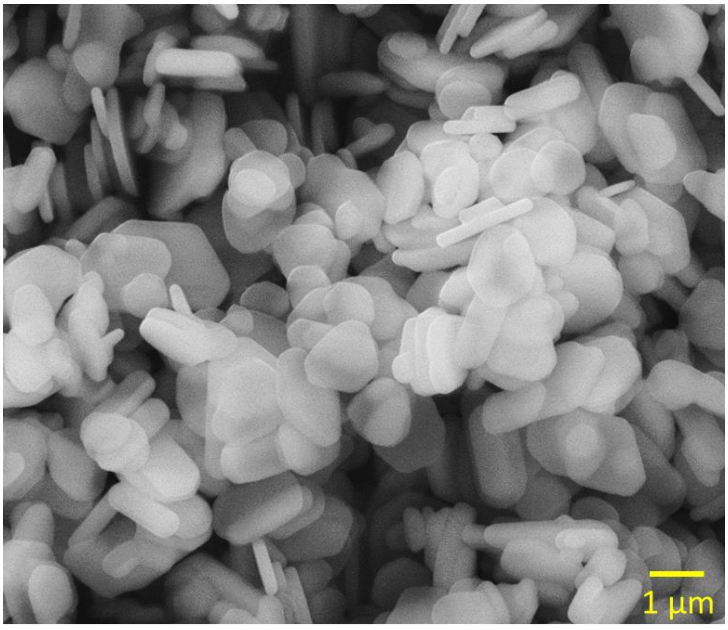

Figure 15. The SEM image of pristine α-ZrP prepared from zirconyl chloride octahydrate via hydrothermal reaction in 12 M H_3PO_4 at 200 °C for 24 h

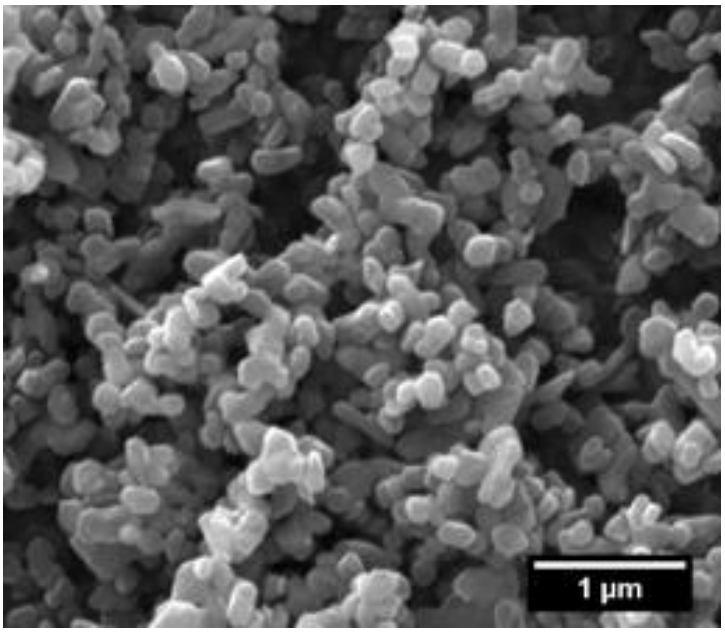

Figure 16. The SEM images of pristine α-ZrP prepared from zirconyl chloride octahydrate via reflux method in 3 M H_3PO_4 at 95 °C for 24 h.

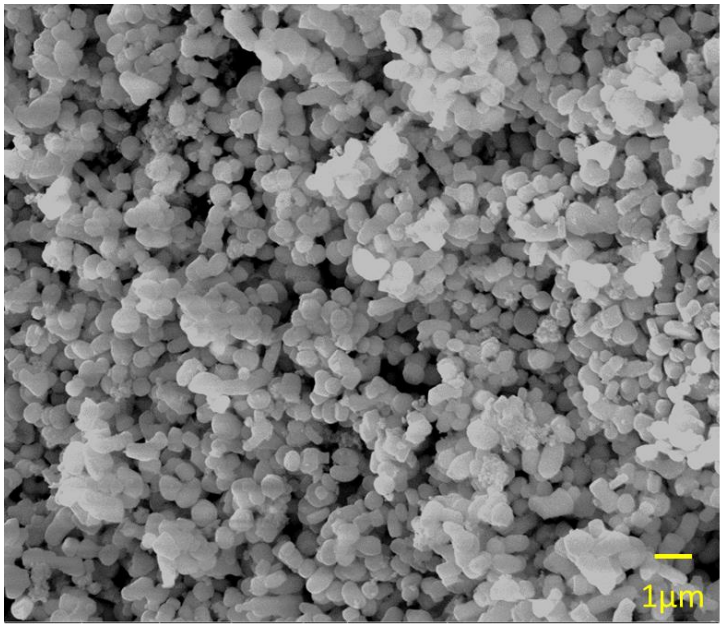

Figure 17. The SEM image of pristine α-ZrP prepared via microwave-assisted method in 15 M H_3PO_4 for at 200 °C for 1 h

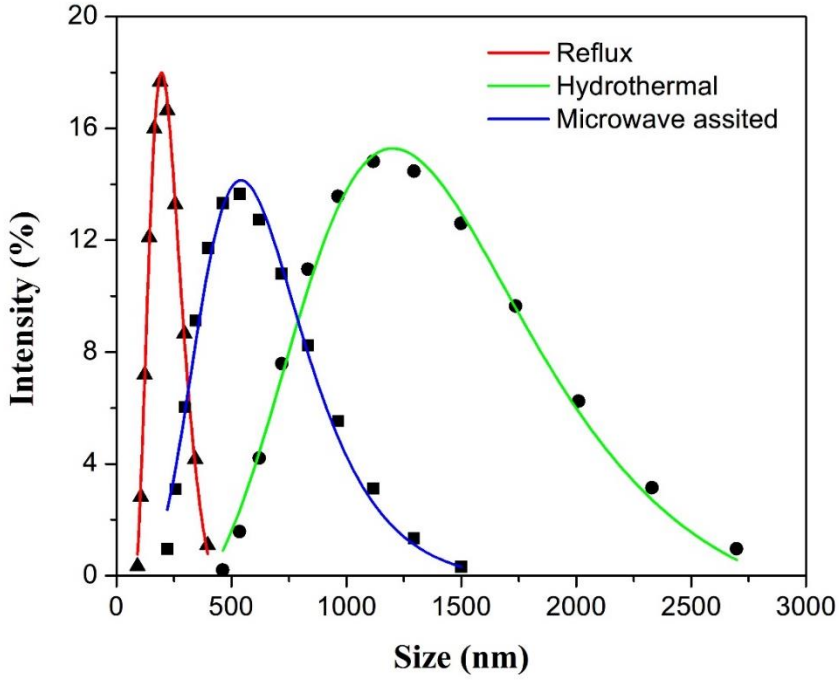

Figure 18. DLS nanodisks size analysis for exfoliated ZrP suspensions prepared by hydrothermal, reflux, and microwave-assisted methods.

formed without stirring. The existence of the gel will result in non-uniform nanodisks or nanodisks with low crystallinity.

The microwave-assisted method is an emerging technique for nanomaterial synthesis. In a general microwave-assisted synthesis of ZrP procedure, water serves as a medium microwave absorber [64], which is able to efficiently convert microwave energy into heat. When water molecules are being irradiated by microwave, the dipoles in water molecules tend to align themselves with the applied electromagnetic field accordingly. As a result, energy from dielectric heating and friction between water molecules is released as heat. Thus, heat is generated internally, and is more efficient than external heat transfer that takes place in conventional oven. In microwave-assisted method, a relatively low

reaction temperature (150 ˚C) and shorter reaction time (10 min and 60 min) are found to result in desired size of α-ZrP. Figure 19 shows the TEM images of α-ZrP crystals made by microwave-assisted method. It was observed in Figure 19a that some crystals were formed after 10 min of microwave dielectric heating. Although some well-defined hexagonal shapes of α-ZrP could be found, most of the obtained crystals are neither regular in shape nor uniform in size. When reaction time was increased from 10 min to 60 min, a sharp and regular shape of α-ZrP crystal was formed, indicating better crystallinity of the final products. In this study, required reaction time for synthesis of α-ZrP is significantly reduced with assistance of microwave dielectric heating from days to less than an hour. Therefore, a quick evaluation of parameters and design for fabrication of nanomaterials could be achieved by microwave-assisted method.

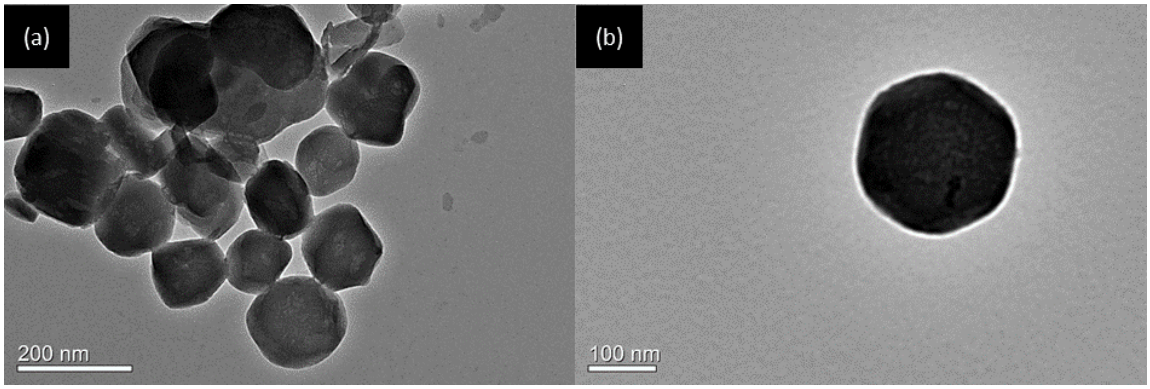

Figure 19. TEM images of the microwave-assisted growth of α-ZrP crystals at 150 ˚C for (a) 10 min and (b) 60 min.

A schematic illustration of the exfoliation process of multilayer crystal into monolayers is shown in Figure 20. The physical appearance of exfoliated suspension is

pearly white (Figure 21) while that of unexfoliated suspension is turbid white. In order to check stability of the dispersion of ZrP nanodisks, the dispersion solution was centrifuged for an hour at high (4000 rpm, 2500 x g) rotation speed. However, no sedimentation was observed which proved that dispersions in water are stable due to repulsion force of surface charges on ZrP nanodisks. The exfoliated samples after centrifugation sometimes give very small amount of sediment on account of partially exfoliated ZrP. Top part is considered as well-exfoliated. Liquid-crystalline phases of exfoliated ZrP nanodisks are interesting because of highly anisotropic (thickness to size ratio is very small) nature and electrostatic interactions between nanodisks. Isotropic to nematic transition is observed at very low volume fractions of ZrP because of high anisotropy. Nematic tactoids nucleate, grow and settle due to gravity. As a result, nematic phase is formed at the bottom as can be seen in Figure 22.

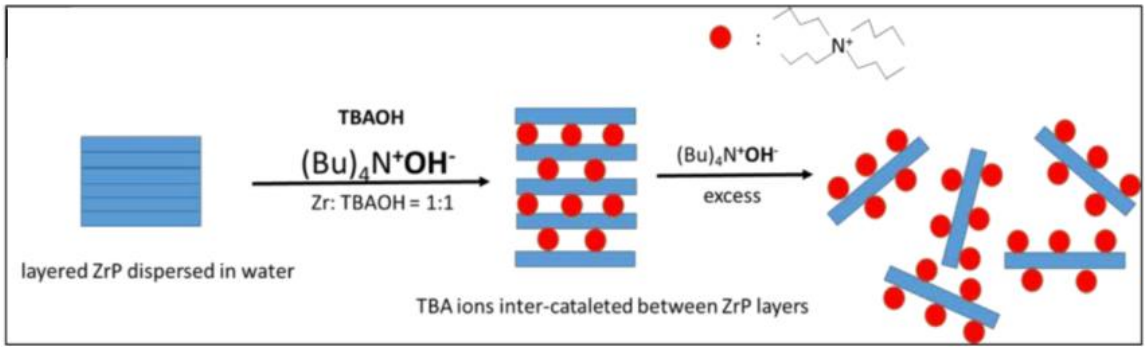

Figure 20. Schematic of process of exfoliation of layered zirconium phosphate using tetra (n) butyl ammonium hydroxide, TBA^+ ions, cover ZrP disk on either sides. Overall charge in the system is zero as oxygen on surface of disks carries a negative charge. At ZrP:TBAOH molar ratio 1:1, almost all TBA^+ ions are on the surface of ZrP. As the amount of TBA^+ ions are increased, TBA^+ ions surround ZrP disks from both sides. Inset shows the electrostatic interaction between oxygen (part of ZrP) and TBA^+ ions on the surface of nanodisks.

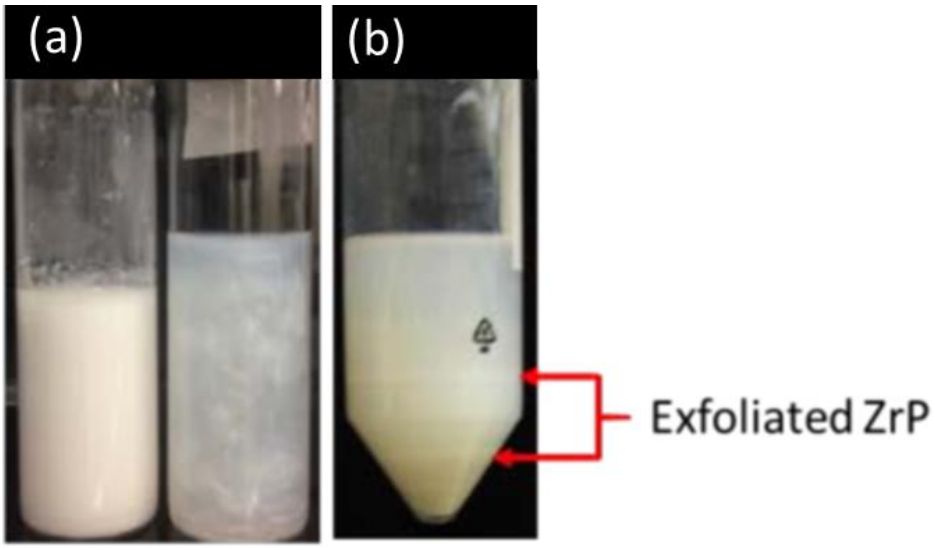

Figure 21. (a) Unexfoliated (left) and exfoliated (right) α-ZrP suspensions and (b) Exfoliation and fractionation of α-ZrP prepared from reflux method and only exfoliated ZrP in the middle layer is collected (as marked).

Figure 22. ZrP nanodisks suspensions with increasing concentrations from left to right observed between crossed polarizers. Volume fraction of the nanodisks from left to right: 0.38%, 0.44%, 0.50%, 0.53%, 0.56%, 0.63%, 0.75% and 1% respectively. The colorful portions indicate nematic ordering of disks. Due to gravity, nematic tactoids settle at the bottom. This picture is taken after 3 days of gravity sedimentation of nematic tactoids.

3.5 Conclusion

The long time effect of gravity causes compression of crystals which is currently being studied in our lab. Due to charges on the surface, the electrostatic interactions between nanodisks play an important role in determining the self-assembly of nanodisks. The complete phase diagram of naturally abundant nanodisks is yet to be fully understood. Besides the formation of the liquid crystalline phases [67], ZrP has potential applications in drug delivery [70]. Monolayer ZrP is a good candidate as the nanodisks for nanocomposites, such as thin film [71].

CHAPTER IV

INTERFACIAL STABILIZATION BY NANODISKS*

4.1 Synopsis

It is the first time that a rapid microwave-assisted method was systematically investigated to synthesize alpha phase of zirconium phosphate (α-ZrP). The dimension and thickness of α-ZrP nanodisks were varied by altering the concentration of added phosphoric acid. In addition, laminar structure of α-ZrP can be exfoliated into monolayers to provide with more surface area by intercalating tetrabutylammonium hydroxide. The results revealed that uniform and highly-crystallized α-ZrP nanodisks were obtained in an efficient manner and could be utilized as a Pickering emulsion stabilizer after exfoliation.

4.2 Introduction

Alpha phase of zirconium phosphate (α-ZrP) has been well studied as an acidic layered metal salt whose lattice structure is depicted in Figure 23a, where each layer of α-ZrP is composed of a ZrO_6 sheet coordinated with HPO_4^{2-} tetrahedrons forming a covalent network and ZrO_6 layers are packed by Ver der Walls forces [72, 73]. By intercalating guest species into the interlayer spacing (shown in Figure 23b), the α-ZrP could serve as a host structure [74] be exfoliated by the guest species. The modified α-ZrP has connected to new applications such as drug delivery [75], foams [76, 77], and Pickering emulsions

*Reprinted with permission from "Microwave-assisted rapid synthesis of hexagonal α-zirconium phosphate nanodisks as a Pickering emulsion stabilizer" by Y.-H Yu, Y.-P Chen, Z. Cheng, 2016. Materials Letters, 163, 158-161, Copyright [2016] by Elsevier.

[78]. In general, α-ZrP could be obtained from hydrothermal, reflux, or hydrofluoric acid assisted methods [79, 80]. However, growth of α-ZrP through a facile and rapid microwave-assisted synthesis with good control over size and uniformity is scarcely reported in literatures.

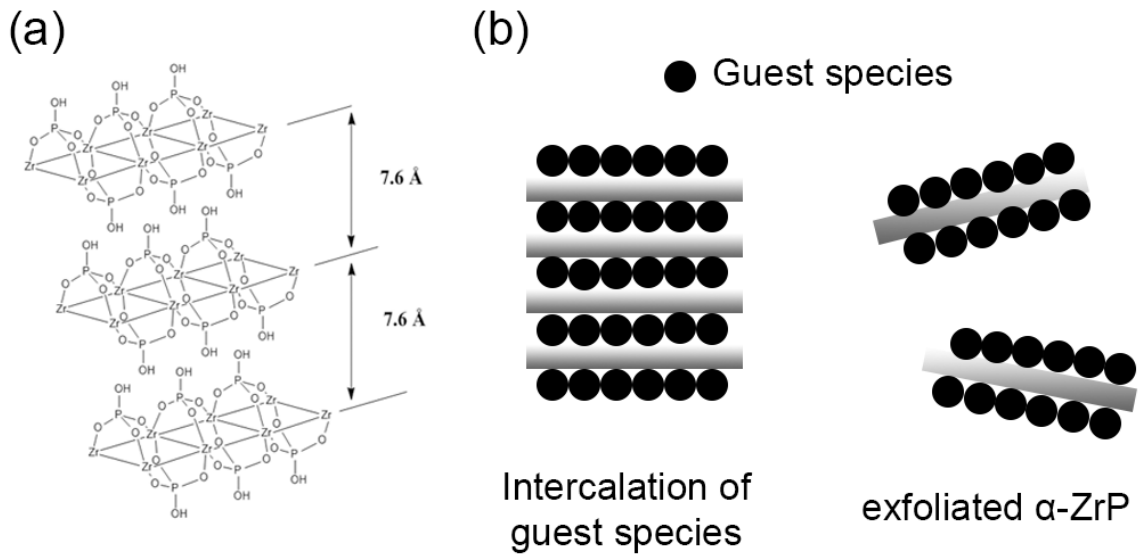

Figure 23. (a) Lattice structure of α-ZrP crystal. (b) Schematic illustrations of the guest species intercalated into α-ZrP interlayers and exfoliated laminar α-ZrP layer-by-layer.

Microwave heating has been typically used in organic chemistry for decades, but not been used for growth of nanomaterials until recent years [81]. The merits of microwave techniques are with efficient heating and instantaneous controllable parameters in real time. When reaction solution is irradiated by microwave power, dipoles existing in molecules are trying to align themselves accordingly to the applied electromagnetic fields. As a result, heat is generated from frictions between molecules and that is more efficient

in terms of heat transfer compared to traditional heat convection used in hydrothermal and reflux methods. Hence, the growth of crystals could be significantly accelerated and well-controlled.

Pickering emulsion was named after Pickering and coworkers' pioneering work over an century ago using solid particle as an emulsion stabilizer [82] whose function is similar to molecular surfactants. Nanomaterials act as barriers to prevent from destabilization because the energy required for removing nanomaterials from surface of emulsion droplet is several orders higher than that stabilized by molecular surfactant [83]. In addition, two dimensional nanomaterials show better stability of formed emulsion droplets by reducing transport of molecules from interior phase [14]. Recently, Pickering emulsion also has been used for polymerization [84], encapsulation [85], and pharmaceutical applications [86].

In this research, to the best of our knowledge, it is the first time that α-ZrP with high uniformity and crystallinity was prepared from microwave-assisted method and the application of α-ZrP nanodisks as Pickering emulsion stabilizer was also demonstrated.

4.3 Materials and Methods

4.3.1 Materials

All chemicals were of analytical grade and used as received without any further purification. Zirconyl chloride octahydrate ($ZrOCl_2 \cdot 8H_2O$) and phosphoric acid (H_3PO_4) were purchased from Fisher Scientific Corp. Dodecane (androus CH_3-$(CH_2)_{10}CH_3$), polystyrene ($(C_8H_8)_n$), and Azobisisobutyronitrile (AIBN) was purchased from Sigma-Aldrich.

4.3.2 Preparation of ZrP nanodisks

1 g of zirconyl chloride octahydrate ($ZrOCl_2 \cdot 8H_2O$) was mixed with 10 mL of 6.0/9.0/12.0 M phosphoric acid (H_3PO_4) under vigorous stirring (hereafter marked as ZrP-6M, ZrP-9M, and ZrP-12M, respectively). The resulting solutions were introduced into a 20 mL glass vessel specified for microwave oven (Discover SP, CEM) and then irradiated by 2.45 GHz microwave at 170 °C for 1 hour. After the microwave-assisted hydrothermal synthesis, the as-synthesized ZrP was washed for three times with deionized water and collected by using a centrifuge. The obtained products were dried in an oven at 65 °C overnight and grinded into fine powders by a mortar and pestle.

4.3.3 Exfoliation of α-ZrP nanodisks and preparation of emulsion droplets

Tetrabutylammonium hydroxide (TBAOH) was served as exfoliation agent. In a typical procedure, molar ratio of ZrP:TBAOH (1:1) was selected to ensure completely exfoliation. 1 g of obtained ZrP was mixed with 2.213 mL of TBA and 25.967 mL of DI water under vigorous stirring for 24 hours. For preparation of Pickering emulsion, 2 mL of dodecane was added to 2 mL of 1 wt% exfoliated ZrP nanodisk suspensions, and then emulsified with a sonication probe (Sonifier 250, Branson) for 10 sec at 10 % of power.

4.3.4 Pickering emulsion polymerization by ZrP nanodisks

The Pickering emulsion polymerization of styrene was performed by exfoliated ZrP suspensions at a constant volumetric fraction of liquid/monomer styrene and AIBN was used as initiator for polymerization. The Pickering emulsion was generated with assistance of a probe sonication in 5 sec and were subsequently polymerized in an oven at 65 ^oC overnight.

4.3.5 Characterizations

Powder X-ray diffraction (XRD) patterns of the as-prepared samples were analyzed on Bruker-AXS D8 Advanced Bragg–Brentano X-ray powder diffractometer. The morphologies were observed by field emission scanning electron microscopy (FE-SEM, Quota 600, FEI) and transmission electron microscopy (TEM, JEM-2010, JEOL) operated at an accelerating voltage of 200 kV. The size distribution of ZrP nanodisks was analyzed by a dynamic light scattering analysis (DLS, Zetasizer Nano ZS90, Malvern). Optical microscopy was performed with scanning laser confocal microscopy (ECLIPSE Ti, Nikon).

4.4 Results and Discussion

Microwave-assisted heating profile (shown in Figure 24) was first examined to ensure the synthesis condition was well-controlled. It was observed that the predetermined-temperature was rapidly reached in only a few minutes. In addition, the heating profile also showed that the reaction temperature was well-kept without generating obvious thermal fluctuation. After microwave-assisted hydrothermal process in different concentration of phosphoric acid at 180 ^{o}C for 1 hour, the crystal phases of ZrP nanodisks were identified by XRD (Figure 25). The XRD patterns of as-synthesized ZrP showed sharp characteristic peaks corresponding to alpha phase of ZrP based on JCPDS card No. 34-0127, suggesting good crystallinity of obtained ZrP after 1 hr of microwave heating. It is also noticeable that relative peak intensity of (110) to (112) increased with concentration of phosphoric acid. This growth mechanism of α-ZrP could be described that the growth rate along (001) plane is getting faster in the phosphoric acid of a higher concentration,

and also would restrain the growths along other crystalline planes, which is in a good agreement with the result reported by our group previously [72].

Figure 26 (a-c) show SEM and TEM (d-f) images of α-ZrP prepared from phosphoric acid of different concentrations. It was observed that α-ZrP nanodisks were hexagonal in shape and their thickness increased as concentration of phosphoric acid increased. The insert SEM image in Figure 26c reveals a zoomed-in image showing layered structure of α-ZrP on the bottom left. It presents an important property that the number of interlayer spacing and overall surface area provided by individual α-ZrP nanodisk could be tailored through controlling the concentration of phosphoric acid.

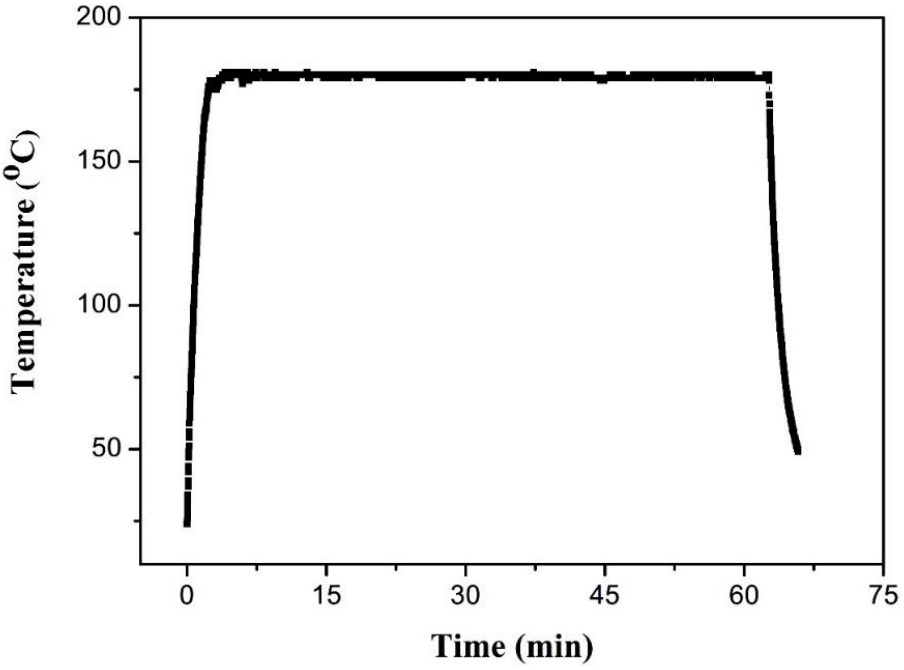

Figure 24. Microwave-assisted heating profile

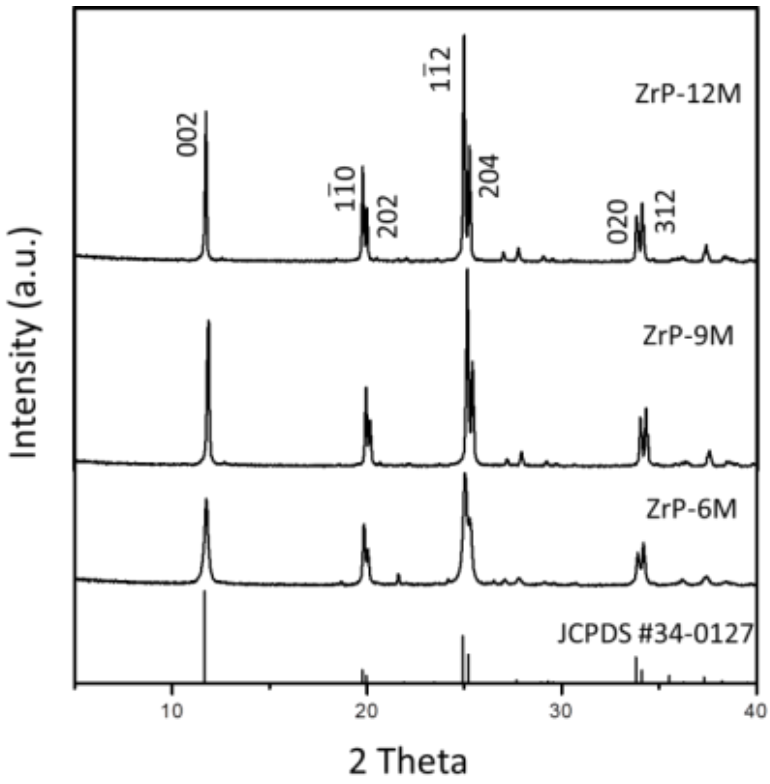

Figure 25. X-ray diffraction spectra of α-ZrP treated with H_3PO_4 of various concentrations, (from top) ZrP-12M, ZrP-9M, and ZrP-6M.

Figure 27 shows that the average size of α-ZrP obtained from 6.0M/9.0M/12.0M phosphoric acid are 196.3 ± 55, 307.8 ± 83, and 324.8 ± 95nm with polydispersity index of 0.17, 0.074, and 0.129, respectively, The highly uniformity of each obtained α-ZrP nanodisks is indicated; in addition, the result is very promising because synthesizing anisotropic nanomaterial has always been a very challenging task.

Figure 28(a-c) show the emulsion droplets stabilized by above mentioned three exfoliated α-ZrP nanodisks. The formed emulsion type is classified as water-in-oil (W/O) emulsion owing to hydrophilic characteristics of α-ZrP nanodisks and TBAOH. It is worth noting that the existence of hydroxyl groups on the surface makes α-ZrP be functionalized

by hydrophobic organic compounds through covalent bonding; that is, the hydrophobicity of α-ZrP nanodisks could be tailored depending on functional groups and desired applications. It could be also found that the diameter of generated emulsion droplets is around 1 μm or even smaller and would be stable for days. Figure 28d is a schematic illustration of W/O emulsion droplet stabilized by α-ZrP nanodisks. In order to realize the impact of the uniformity of ZrP nanodisks on the formed emulsion droplets stabilized by Pickering emulsion, we performed polymerization of styrene using exfoliated ZrP nanodisks. The TEM images (Figure 29) showed that the formed polystyrene particles were uniform in size and spherical in shape. In our previous work [78], the polystyrene particles stabilized by hydrothermal-made Janus ZrP were larger in size and more facets on the edges. The advantage of uniform ZrP nanodisks as a Pickering emulsion stabilizer is that uniform emulsion droplets are formed without altering wettability of ZrP nanodisks.

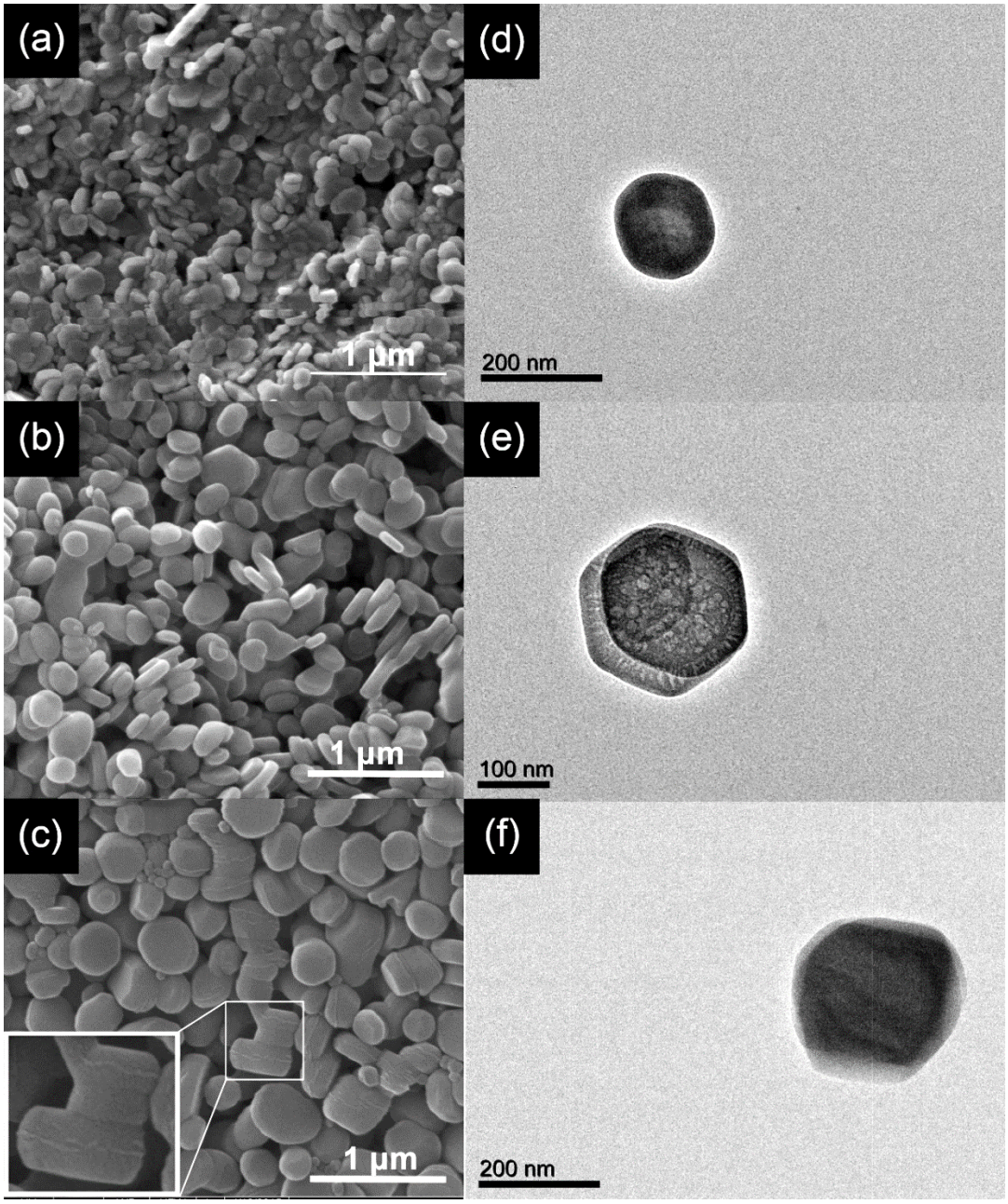

Figure 26. SEM (a-c) and TEM (d-f) images of α-ZrP synthesized in different H_3PO_4 concentrations: 6M, 9M, and 12M, respectively.

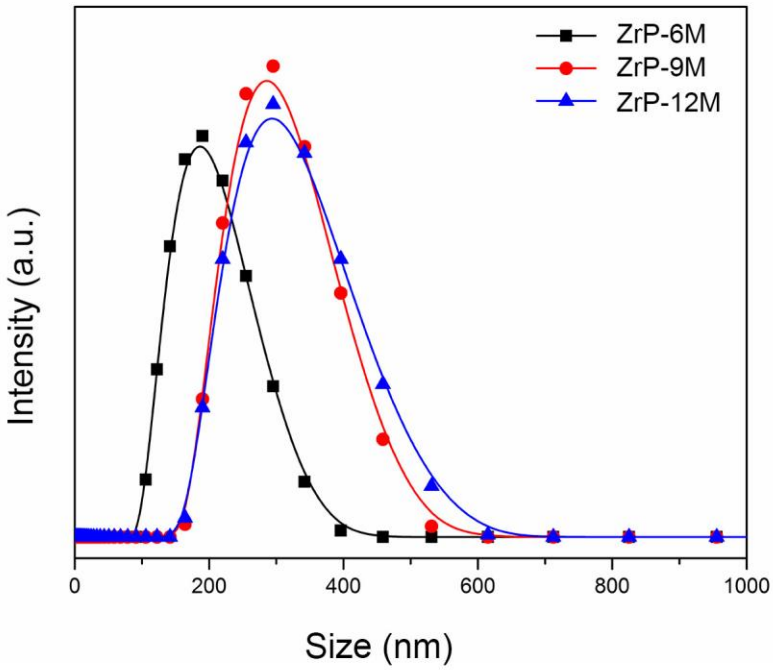

Figure 27. The size distribution of these nanodisks.

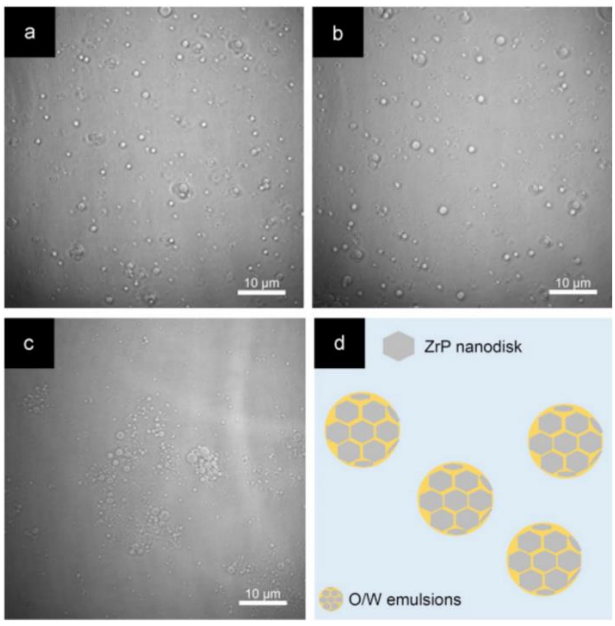

Figure 28. Scanning laser confocal microcopy images in bright field of water-in-oil emulsion droplets stabilized by exfoliated (a) ZrP-6 M, (b) ZrP-9 M and (c) ZrP-12 M, and (d) the schematic illustration of O/W emulsion stabilized by α-ZrP nanodisks.

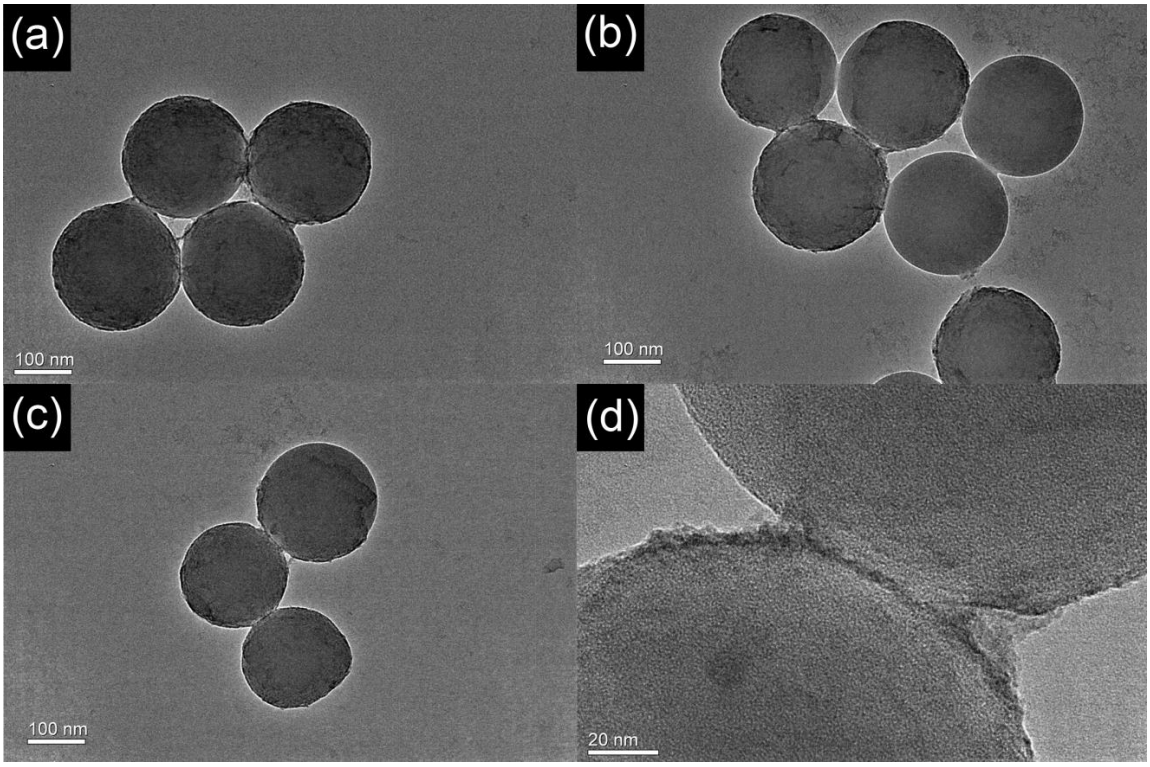

Figure 29. Representative polystyrene particles stabilized by (a) exfoliated ZrP-6M, (b) exfoliated 9M, (c) exfoliated 12M nanodisks, and (d) interface of two adjacent polystyrene particles stabilized by exfoliated ZrP-3M nanodisks.

4.5 Conclusions

It is the first time that uniform and highly-crystallized hexagonal α-ZrP nanodisks were prepared through a microwave-assisted synthesis route. The average size of obtained α-ZrP nanodisks was approximately 200-300 nm with very low polydispersity index indicating good uniformity and high consistency. The structures and dimensions of α-ZrP nanodisks were characterized by XRD, SEM, TEM and DLS; furthermore, the analyses show good agreement with previous studies. This facile and rapid technique provides with now only a new approach to produce high quality α-ZrP, but also shows the application

serving as a Pickering emulsion stabilizer that may be useful for further developing applications in various fields.

CHAPTER V

JANUS ZRP NANODISKS FOR ENHANCED OIL RECOVERY

5.1 Synopsis

Decreasing size of two-dimensional nanodisks are of greatest interest for enhanced oil recovery (EOR) due to formation of extremely stable emulsion droplets and resistance to harsh condition in oil reservoir. Synthesis methods of ZrP including hydrothermal, reflux, and new microwave-assisted methods have been systematically investigated in previous chapter. We found that smaller size of ZrP could be obtained from reflux method by using different reagents and solvents. Several conventional solvents were used to development of nanosize ZrP and a commercial available microfluidic device was performed for evaluation of EOR.

5.2 Introduction

Recently, many attention has drawn to study EOR using microfluidic devices that enable visualization of mechanism of oil recovery. Prototype models and network made of transparent (or translucent) materials, such as glass and polydimethylsiloxane (PDMS), are typically used to pattern rock channel. Porous micro-models of media in silicon, glass, PDMS, and other polymer devices have been used for better understanding of multiphase fluid transport at the pore-level scale. Real-time, in situ observation of relevant fluid transport in complex systems involving multiple phases and pore geometries are allowed by micro-model systems.

The innovation of using microfluidic model to study EOR is not mainly focusing on the tiniest dimension that can be patterned on chip, but on how the pattern is analogous to the structure of rock in oil reservoir. Recently, researchers used regular pattern with cylindrical pillars to study the oil removal mechanisms by various EOR methods. For example, de Haas et al. used a lab-on chip approach to study steam assisted gravity drainage (SAGD) that is a thermal process by injecting steam into oil field, reducing viscosity of crude oil, causing the heated oil to drain into the lower wellbore [87]. In their study, the microfluidic chip was made through a series of step including mask-making, etching the glass substrate and device assembly. Ma et al. also developed their microfluidic chip using silicon wafer coated with SU-8 50 photoresist, and maskless photolithography to study foam sweep [88]. The real-time observation helps understand what happen when EOR agents are injected into the microfluidic chip. However, it can be seen that although the authors claim that grain size, porosity and permeability is similar to that of rock, the much simplified pattern is not a typical case in oil reservoir and limit its application. Therefore, efforts have been made to improve patterning such as assistance of computational software and selection of substrate.

In addition to use microfluidic device, a one-pot synthesis to prepare amphiphilic ZrP nanodisks was inspired and modified from previous work [89]. In the formation process, ZrP was derived from addition of different zirconyl precursor to phosphoric acid in several common solvents with/without heat treatment. The new approach led us to obtain ZrP nanodisks whose size is than 100 nm.

5.3 Materials and Methods

5.3.1 Materials

Zirconyl propionate was donated by Dr. Abraham Clearfield's group. Phosphoric acid (H_3PO_4), Dimethylformamide (DMF, C_3H_7NO), Ethanol (200 proof, C_2H_5OH), and 1-propanol (99+%, C_3H_7OH), Ethylene glycol, Toluene, Octadecyl isocyanate (> 80%, C18-ICN) were purchased from Fisher Scientific Corp. Dodecane (androus CH_3-$(CH_2)_{10}CH_3$) was purchased from Sigma-Aldrich.

5.3.2 Preparation of ZrP nanodisks from different solvent

Clear solutions would be obtained by dissolving 3.3 mmol of zirconyl propionate into 10 mL of methanol, ethanol, and 1-propanol, respectively. Concentrated phosphorous acid (85%) was dropwise added into the clear solutions that would turn into gel in a few seconds. The gel was then transferred into 3 neck round bottom reactor and waited for 15 min until it gelled totally. Once it gelled, 100 mL of toluene was introduced into the reactor to re-disperse the gel. After, dissolved 1.18g of C_{18}-ICN into 10 mL of toluene then added into the reactor. Finally heated reactor to 100 ^oC and 10min vacuum-10 min nitrogen treated 3 times and let it reflux for 24 hr (Figure 30). The exfoliation follows the same procedure in ***3.3.4***.

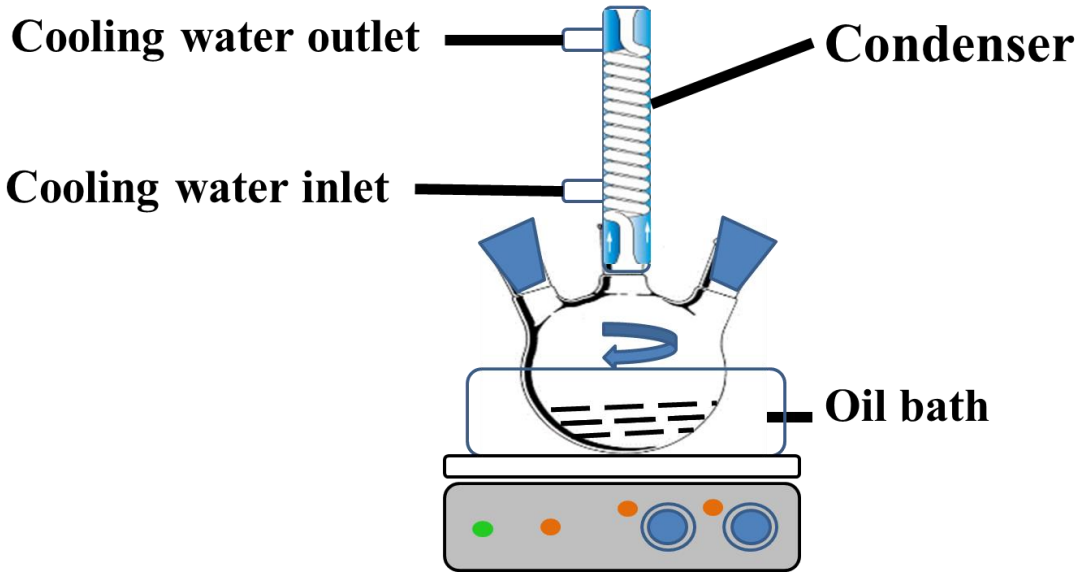

Figure 30. Experimental setup of reflux method.

5.3.3 Characterization

Powder X-ray diffraction (XRD) patterns of the as-prepared samples were analyzed on Bruker-AXS D8 Advanced Bragg–Brentano X-ray powder diffractometer. The morphologies were observed by transmission electron microscopy (TEM, JEM-2010, JEOL) operated at an accelerating voltage of 200 kV.

5.3.4 Study of EOR by using microfluidic device

Microfluidic device provides a convenient and controllable environment for visualizing displacement mechanism at the pore scale. Figure 31 is the profile of the microfluidic chip provided by manufacturer (Trianja tech., *USA*). The microfluidic chip consisted of a porous area of hexagonal flow-cell with 13 mm in length and 10 mm in width and was made of fused silica with two inlets, one hexagonal and one outlet. The experimental setup was shown in Figure 32a. Two syringe pumps were connected to two

inlets for precisely controlling the flow rate of injected formulation. A microscope (10X-250X magnification, 2.0 Mpixel CMOS image sensor) was used to visualize flooding process.

Prior to flooding test, the microfluidic chip was cleaned by DI water, followed by ethanol, blown dry by using air flow and finally dried in oven at 65 ℃. After cleaning process, the chip was checked by microscope to ensure no residual oil or other solvent left inside. In order to differentiate oil/water phases, dodecane and aqueous solution were dyed with nile red and methylene blue, respectively. In the first step, the chip was filled with dodecane in a flow rate of 0.2 mL/hr and saturated overnight to alter the wettability of porous media from water-wet to oil-wet. Several formulations were prepared for flooding test, including water, ZrP nanofluid, and ZrP/surfactant mixtures. The oil recovery was recorded by microscope every 30 second during the flooding and images were analyzed by ImageJ software. The contrast of clean and microfluidic chip partially filled with oil was shown in Figure 32b and c.

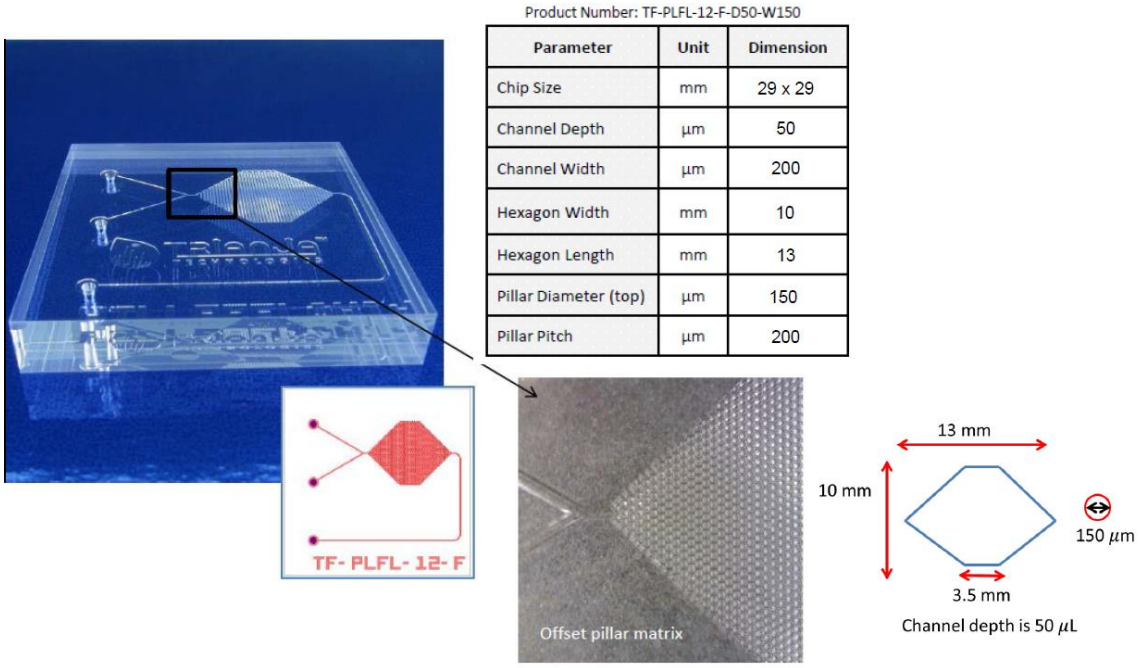

Figure 31. Profile of microfluidic chip

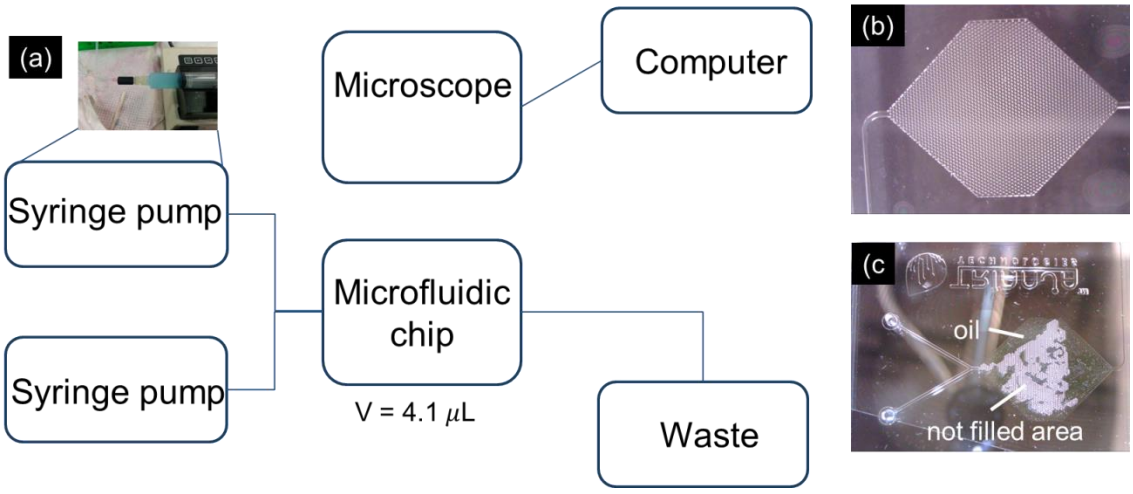

Figure 32. (a) Schematic illustration of experimental set-up, (b) microfluidic chip, (c) microfluidic chip partially filled with dodecane dyed with nile red.

5.4 Results and Discussion

In our effort to synthesize uniform and small sized ZrP nanocrystals, we developed a new synthetic route based on previous work [89]. Other than the solvent used reported in the literature, several more common solvents were used as synthesis medium following the same synthesis condition. In our preliminary results, we synthesized ZrP crystals using different phosphoric acid/zirconium propionate ratio (defined as R and R = 2, 4, and 6 were selected) at low temperature (65 ^{o}C). It is shown in Figure 33 that ZrP crystals synthesized from DMF (a-c), methanol (d-f), ethanol (g-i), and ethylene glycol (j-l) have less-defined regular shapes. Additional solvent, 1-proponal and 2-proponal were selected

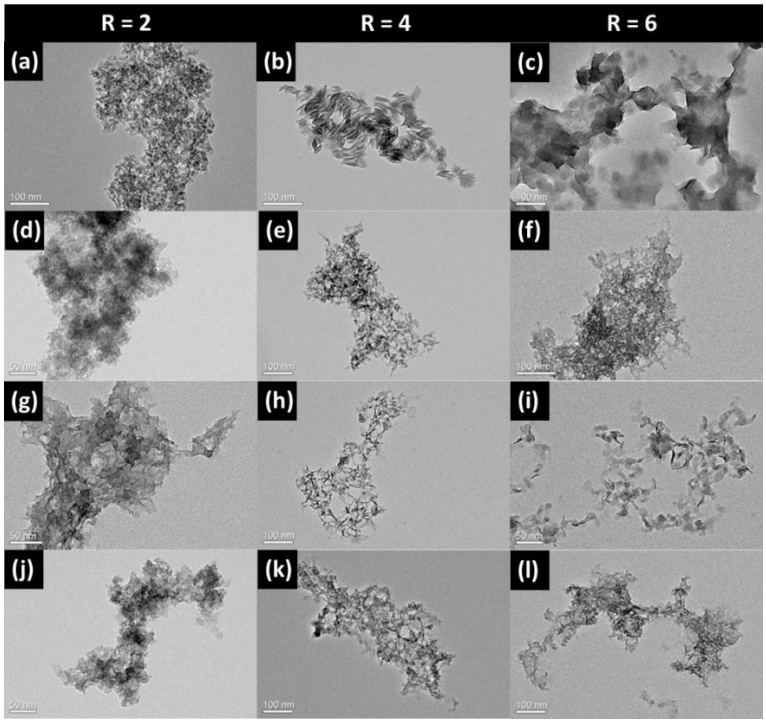

Figure 33. ZrP crystals synthesized from solvent (a-c) DMF, (d-f) Methanol, (g-i) Ethanol, and (j-l) ethylene glycol.

to synthesize ZrP crystals following the same procedure since the zirconium precursors contain propionate group and expected to have better solubility. The representative ZrP crystals were shown in Figure 34. It is obvious that the uniformity and shape regularity of ZrP crystals synthesized from 1-propanol is better than that of 2-proponal, Hereafter, 1-proponal was selected as synthesis solvent for following experiments. The XRD results (Figure 35) also show that the crystallinities of as-synthesized ZrP crystals were low based on the broadening of Bragg peaks. In our previous work, ZrP crystals are usually synthesized at higher temperature (95 – 200 ^{o}C). Therefore, modifications have been made to synthesize ZrP crystals following new procedure but reflux at higher temperature. The

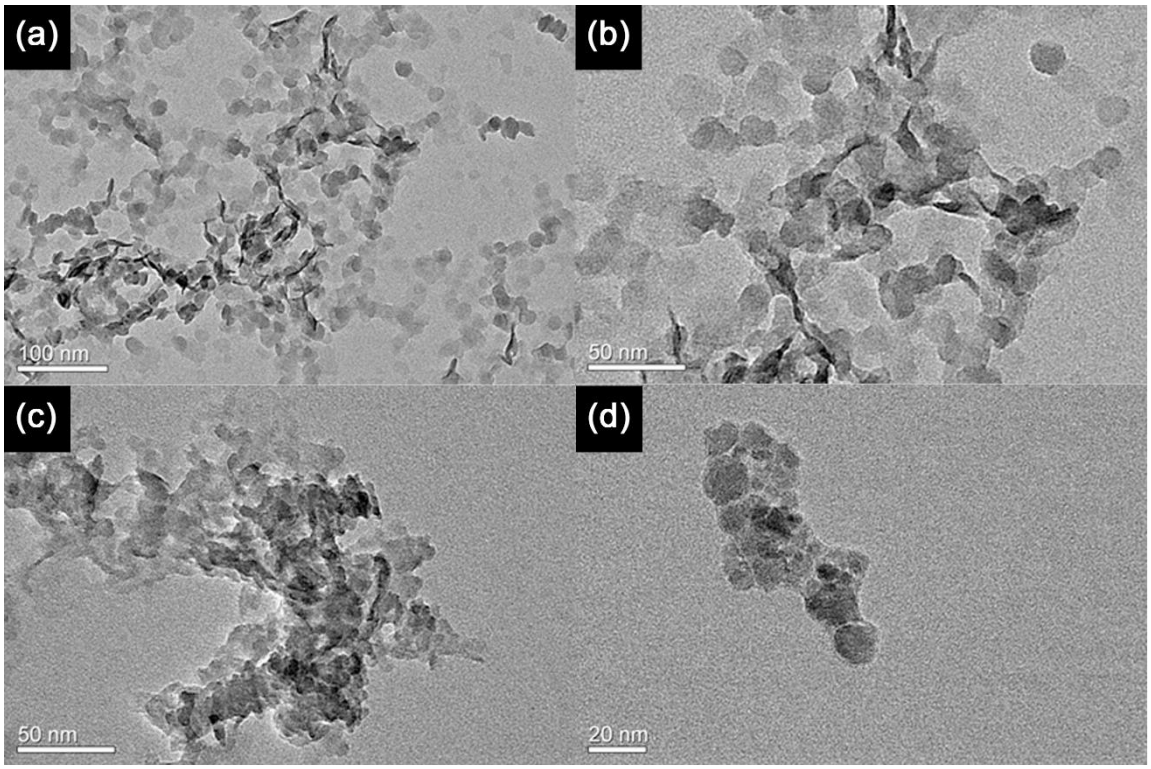

Figure 34. ZrP crystals synthesized from (a-b) 1-proponal, and (c-d) 2-proponal.

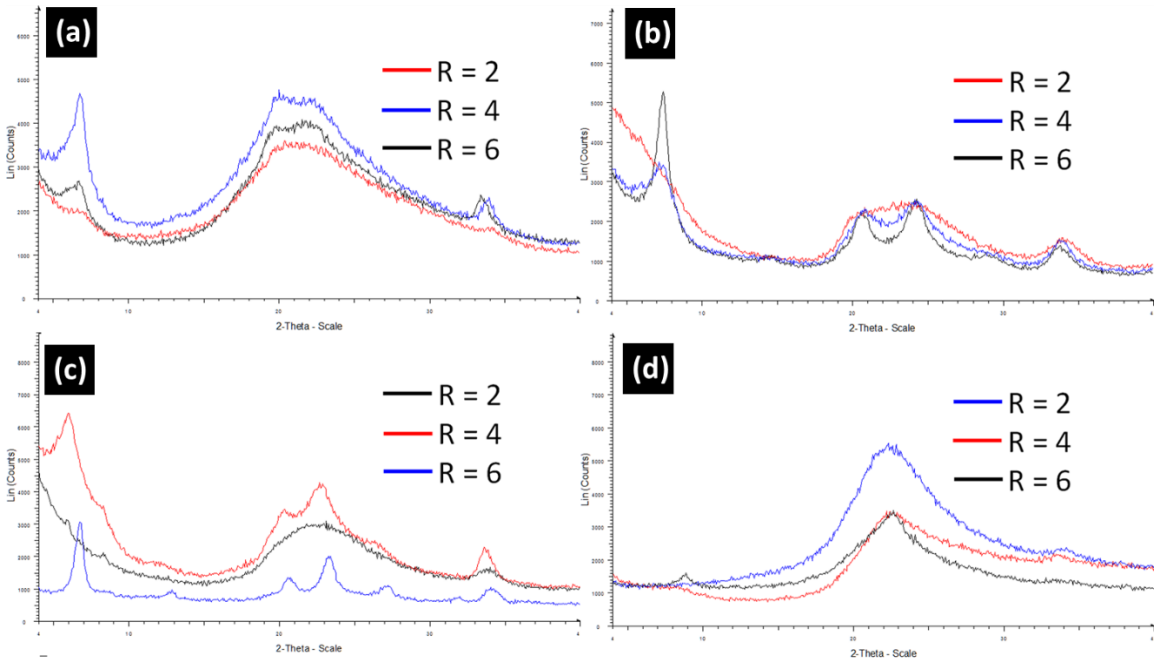

Figure 35. X-ray diffraction pattern of as-synthesized ZrP crystals from (a) DMF, (b) methanol, (c) ethanol, and (d) ethylene glycol.

TEM images of obtained ZrP crystals is shown in Figure 36. More uniform and hexagonal shapes of ZrP crystals can be found, especially for ZrP synthesized from 1-proponal. It also can be observed from XRD pattern of as-synthesized crystals that proves higher temperature helped growth of ZrP crystals. As a result, 1-proponal as a solvent and reflux at higher temperature were adopted as stand synthesis procedure and the obtained ZrP nanodisks were then exfoliated in the same manner mentioned in ***3.3.4*** and diluted to desired concentration as coreflooding fluid.

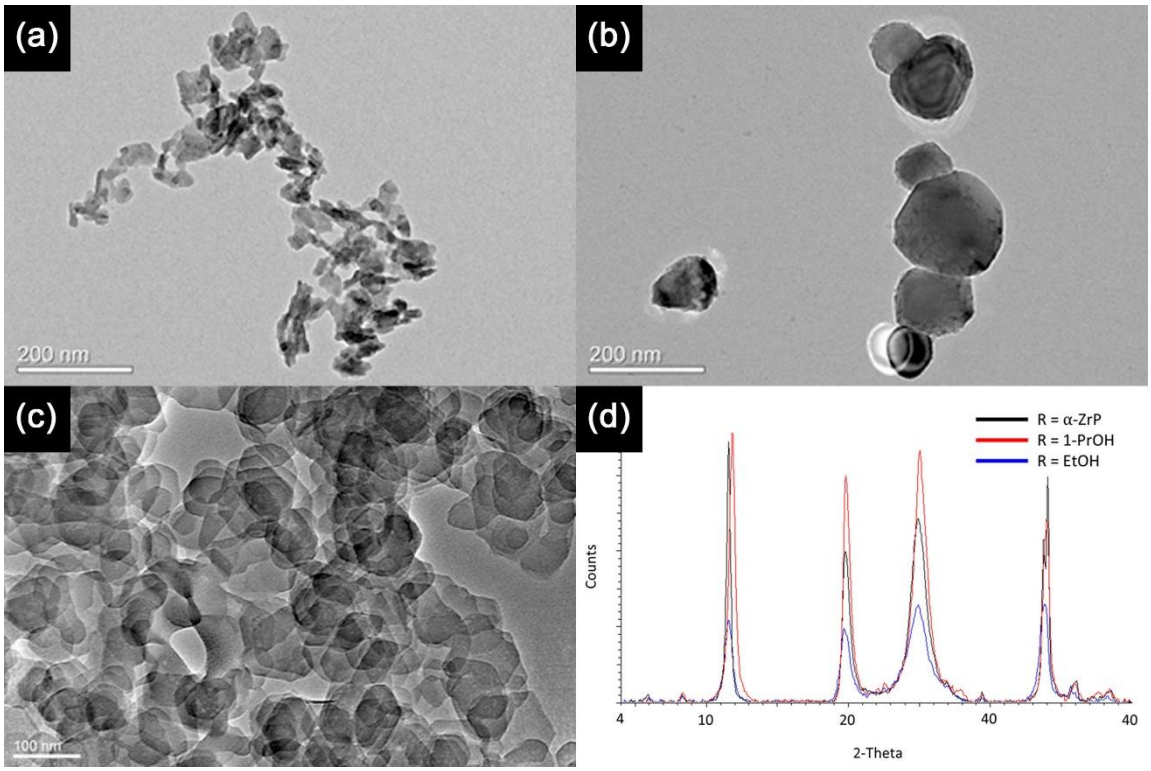

Figure 36. TEM images of ZrP crystals synthesized at 95 ºC from (a) Ethanol, (b) 2-propanol, and (c) 1-proponal, and (d) X-ray diffraction pattern of obtained ZrP crystals.

In order to study the mechanism of water flooding, a slow flow rate at 0.2 mL/hr was selected. Figure 37 is a characteristic curve comparing the fraction of oil recovered with the injected water volume. This plot is similar to a recovery curve in traditional core-flooding experiments. In this case, original oil in place (OOIP) denotes the volume of oil inside the microfluidic chip before waterflooding starts. We observed that less than 30% of OOIP was displaced by injected water in the first stage at a constant flow rate of 0.2 mL/hr. After 8 PV was injected, the oil recovery rate did not improve. When we further increased flow rate to 3 mL/hr, oil recovery rate was enhanced to 43.4 %. It is in agreement with Mai and Kantzas's work. Figure 37 (inset) is a picture of the microfluidic chip

containing dodecane and irreducible water at the end of waterflood. Microscope images were taken at different location of the microfluidic chip shown in Figure 38. It was observed that the pillars showed oil-wet wettability after saturation overnight in Figure 38a and c as expected. It also can be found in Figure 38b and d that oil droplets were displaced by water and flowed in outlet channel. The size of the oil droplets was not uniform with various sizes of tens of micrometer in diameter.

Two formulations of nanofluid containing 0.4 wt% of ZrP with different surface coverage of C18 isocyanate (3% and 33%) were used for the study of mechanism of oil recovery. For comparison, the flow rate was controlled as same as it was used in waterflooding test. It can be observed in Figure 39 that the oil recovery rate was improved by both of nanofluid 20-25% more compared to waterflooding in the first stage. When flow rate increased to 3 mL/hr, 67 % and 68 % of oil recovery rate were obtained by 0.4 wt% of ZrP-C18 (3% coverage) and 0.4 wt% of ZrP-C18 (33% coverage), respectively. Two displacement mechanisms of the residual oil were observed in the microfluidic tests. One is the formation of oil-in-water droplets by Pickering emulsion. Figure 40a shows small and uniform oil droplets were formed in the continuous oil phase and flowed toward water flow, suggesting that functionalized ZrP nanoparticles are able to reduce interfacial tension between oleic and aqueous phases and form emulsion droplets. The other one is called “detergency” resulted from nanoparticles diffusing into solid/oil phase and forming

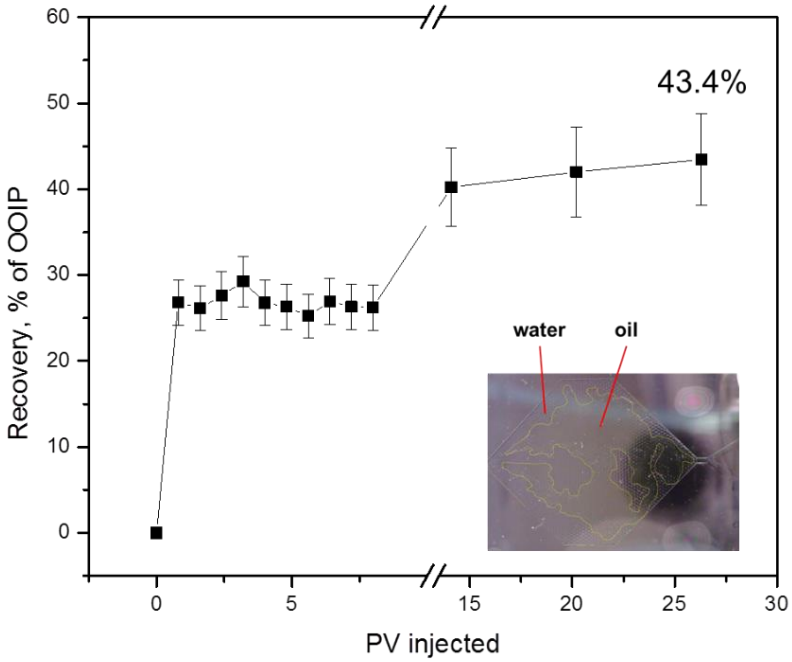

Figure 37. Fraction of oil recovered in terms of original oil in place (OOIP) by injecting water at a constant flow rate of 0.2 ml·hr-1 for 10 min, and then 3 ml·hr-1 for 3 min.

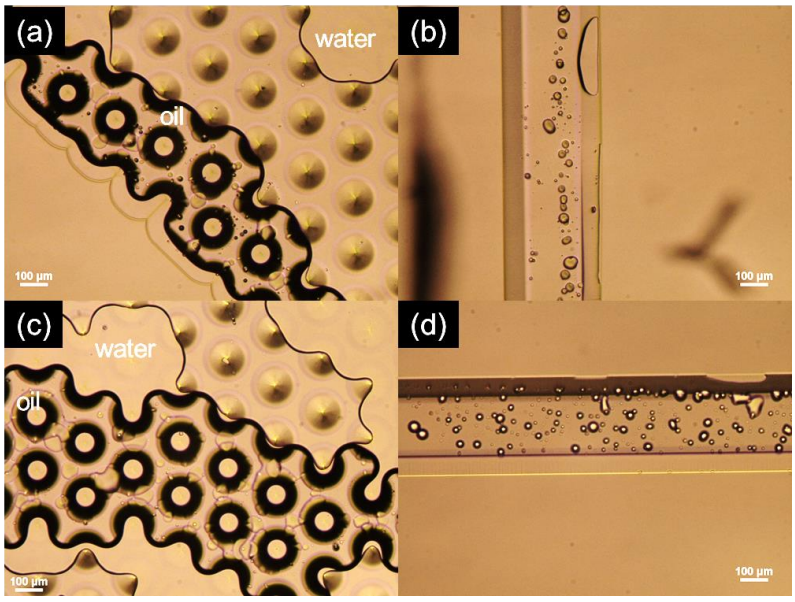

Figure 38. Optical microscope images of microfluidic chip after waterflooding.

a wedge film to remove oil out of solid surface. Figure 40b and c are cross-polarized optical microscopes presenting nanoparticles accumulating at the oil/solid interface. The oil droplets formed by Pickering emulsion were shown in Figure 40. The oil droplets were uniform in size less than 10 μm in diameter, suggesting the nanoparticles functionalized by hydrophobic C_{18}-isocyante helped to stabilize oil-in-water droplets at oil/water interface. Figure 41 shows optical microscope images of microfluidic chip after nanofluid flooding (0.4 wt% ZrP-C18, 33 wt% surface coverage). The oil recovery rate and mechanisms are similar to that of 3 wt% of C18 surface coverage. It also shows both of mechanisms of detergency and reduced interfacial tension between oil and nanofluid, indicating ZrP functionalized with hydrophobic chain is able to improve both of displacement mechanisms.

In order to study the synergism effects of nanofluid and surfactant, 0.01 wt% of APG surfactant was added into nanofluid. Figure 42 shows the oil recovery rate by mixtures of nanofluid and APG surfactant. Additional 15% of recovered oil was achieved by adding little amount of APG surfactant as low as 0.01 wt%. The interfacial tension between oil and mixtures of nanofluid and APG surfactant was dropped from 50 to 0.001 mN/m, indicating that the possible mechanism is reduced interfacial tension owing to appearance of APG surfactant.

Figure 43 and 42 show the optical microscope images of microfluidic chip after flooding by mixtures of nanofluid and APG surfactant. It was observed that interface of oil/aqueous solution was changed and tended to be more miscible due to addition of APG surfactant. More oil-in-water emulsion droplets formed were observed in Figure 43 and

Figure 44. In addition, as expected, the combined mechanisms of oil recovery, detergency effect, Pickering emulsion, reduced interfacial tension, by nanofluid and APG surfactant were observed. Figure 44 shows the comparison of oil recovery rate by all of formulations. Among formulations, it is not surprised that mixtures of ZrP nanofluid (33% of C18 isocyante surface coverage) and APG surfactant showed highest oil recovery rate (81.5 %). The amount of recovered oil is enhanced resulted from participation of nanofluid solution which is ~22 wt% higher than that of waterflood, indicating ZrP nanodisks with higher hydrophobicity not only help to reduce interfacial tension, but also put detergency effect and formation of Pickering emulsion on removing oil from solid surface.

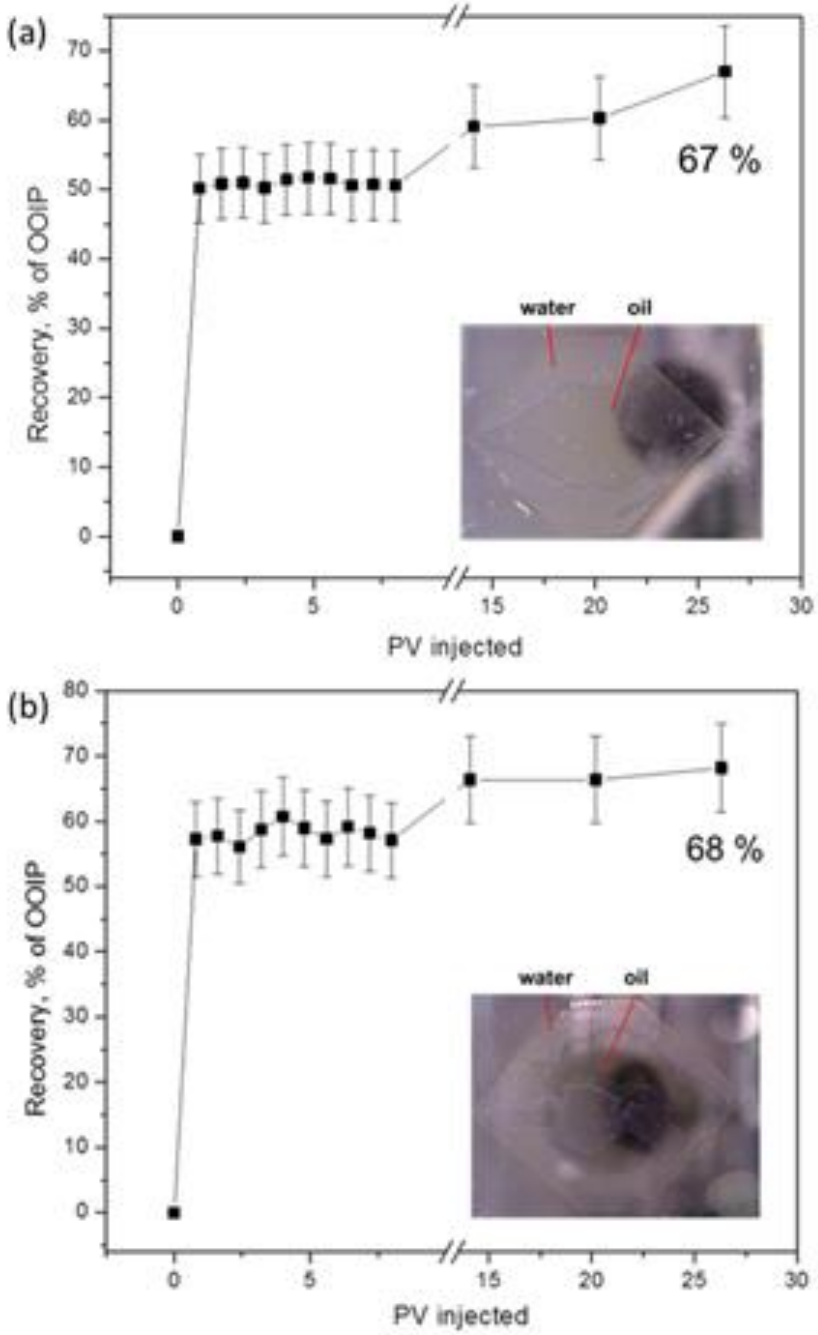

Figure 39. Fraction of oil recovered in terms of original oil in place (OOIP) by injecting (a) 0.4 wt% ZrP-C18 (3% coverage) (b) 0.4 wt% ZrP-C18 (33% coverage) nanofluid at a constant flow rate of 0.2 ml·hr^{-1} for 10 min, and then 3 ml·hr^{-1} for 3 min.

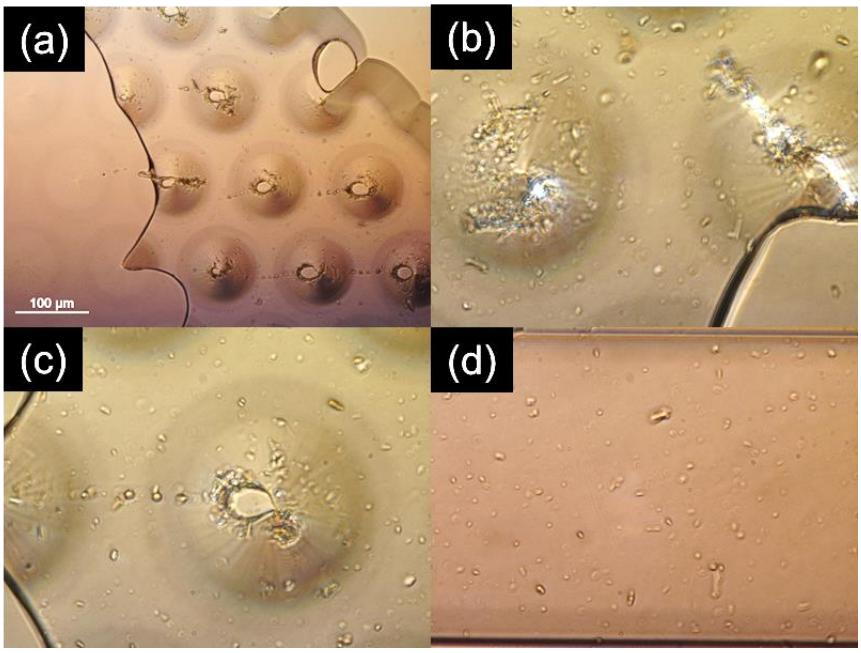

Figure 40. Optical microscope images of microfluidic chip after 0.4 wt% ZrP-C18 (3% surface coverage) of nanofluid flooding.

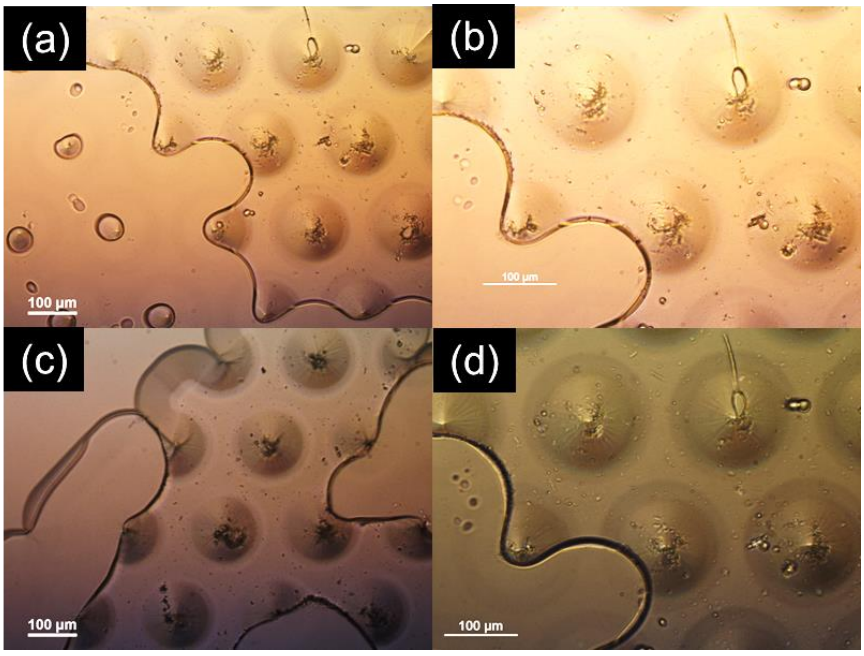

Figure 41. Optical microscope images of microfluidic chip after 0.4 wt% ZrP-C18 (33% surface coverage) of nanofluid flooding.

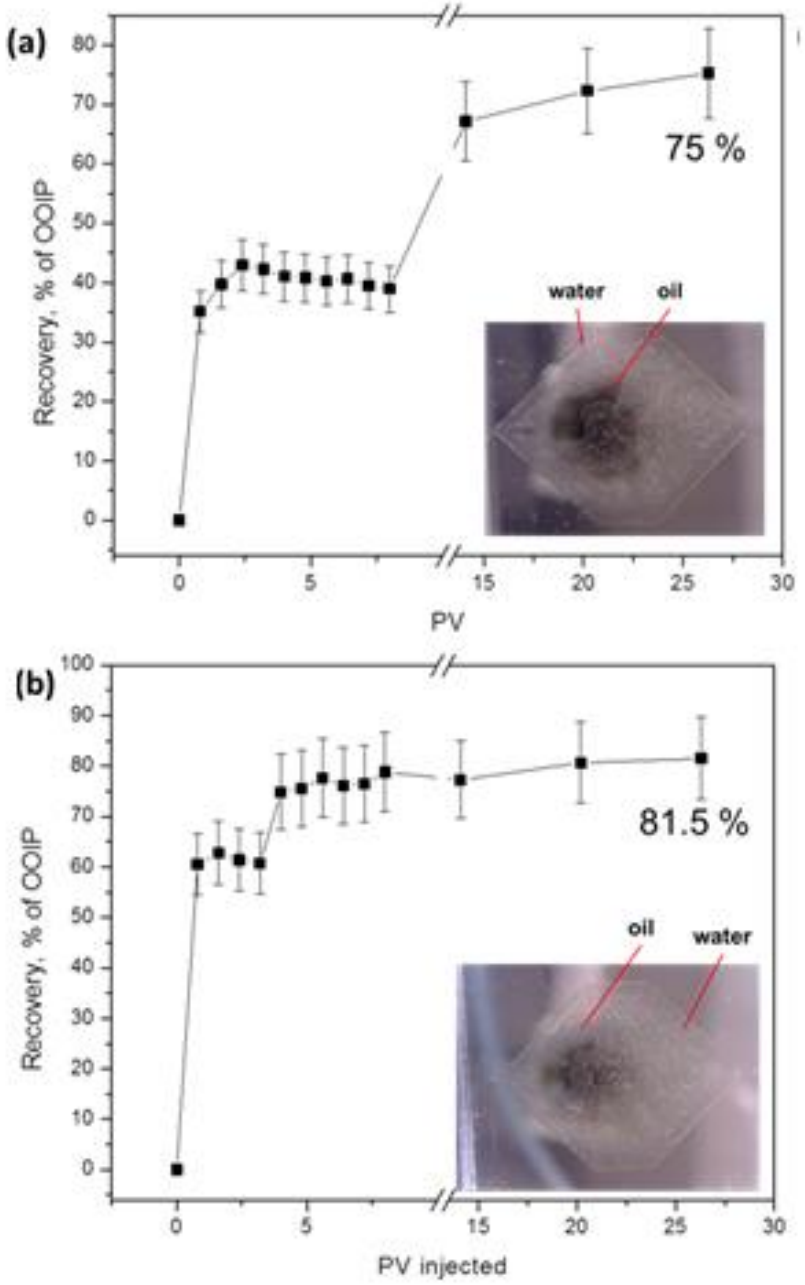

Figure 42. Fraction of oil recovered in terms of original oil in place (OOIP) by injecting formulation of (a) mixture of 0.4 wt% ZrP-C18 (3% coverage) + 0.01 wt% of APG, (b) mixture of 0.4 wt% ZrP-C18 (33% coverage) + 0.01 wt% of APG at a constant flow rate of 0.2 ml/hr for 10 min, and then 3 ml/hr for 3 min.

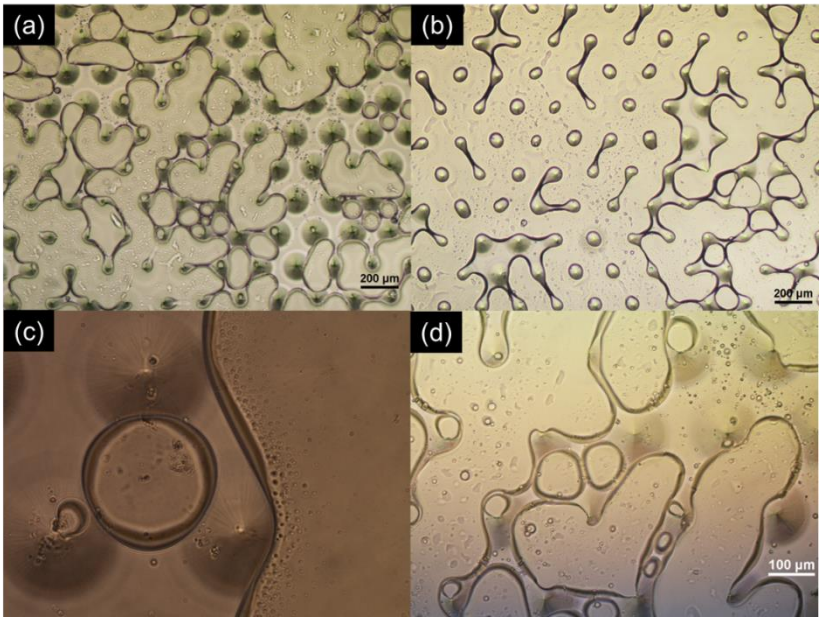

Figure 43. Optical microscope images of microfluidic chip after injecting formulation of mixture of 0.4 wt% ZrP-C18 (3% coverage) + 0.01 wt% of APG.

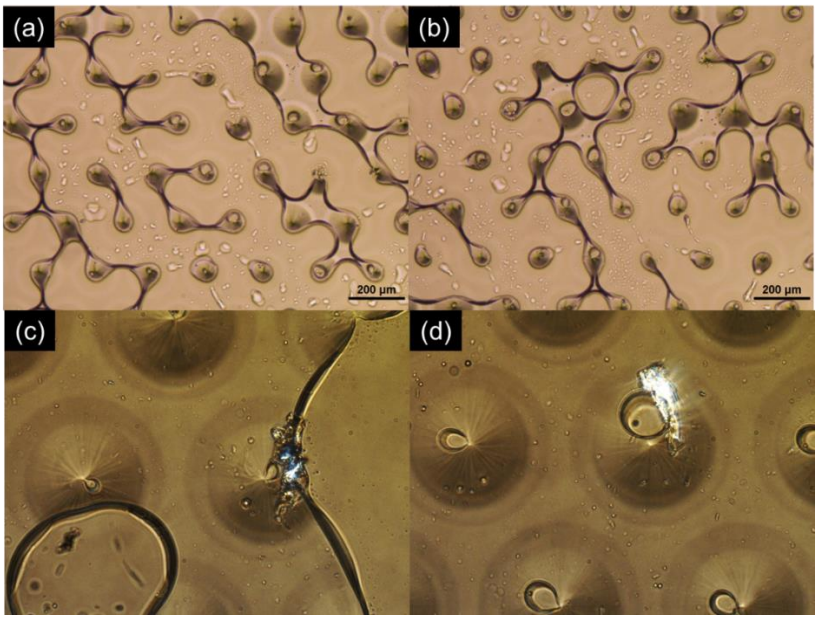

Figure 44. Optical microscope images of microfluidic chip after injecting formulation of mixture of 0.4 wt% ZrP-C18 (33% coverage) + 0.01 wt% of APG. (a)-(b) optical microscope images, (c)-(d) cross-polarized optical microscope images.

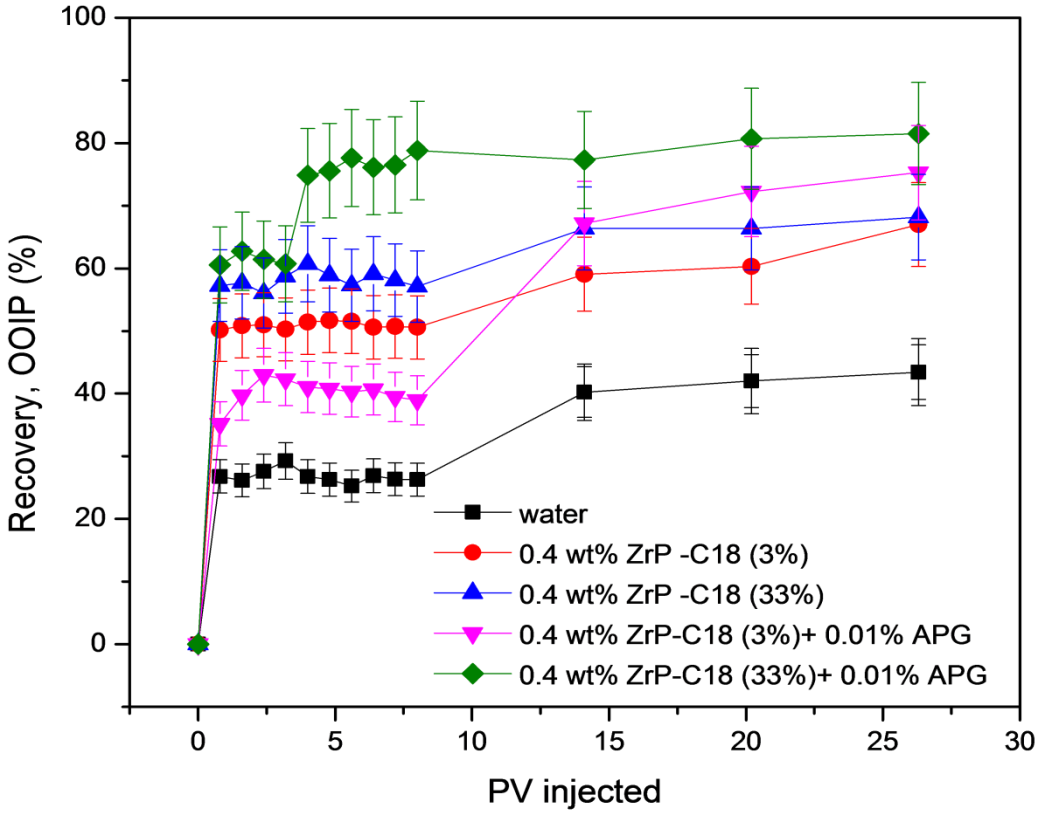

Figure 45. Comparison of fraction of oil recovered in terms of original oil in place (OOIP) by injecting water and 0.4 wt% ZrP-C18 nanofluid at a constant flow rate of 0.2 ml·hr-1 for 10 min, and then 3 ml·hr-1 for 3 min.

5.5 Conclusion

Although study of microfluidic chip has been successful in many fields and provides a quick and controllable environment for rapid assessment, evaluation of enhanced oil recovery by any formulation of surfactant, nanofluid, and mixtures of nanofluid and surfactant with microfluidic devices is still not fully understood. There are still lots of challenges that need to be conquered for using microfluidic chip to study EOR. In general, rock consists of various chemical contents and is different from reservoir to reservoir, but microfluidic chips usually are made of only single material that leads to

simplify the complexities of physical characteristics of rock. For example, the wettability of rock could be changed from upstream to downstream after secondary oil recovery. It is still difficult to make microfluidic chip with water-wet and oil-wet wettability at the same time. Low tolerance to high water pressure/flow rate applied to microfluidic chip might also limit its application because of leaking issue. In addition, although reconstructing 3D pore structures is possible by using microcomputed tomography (micro-CT), focused ion beam-scanning electron microscope (FIB-SEM), nuclear magnetic resonance (NMR) imaging or ultrasonic scanning, these types of simulations are computationally expensive, limited to small sample sizes and not possible to scale-up to actual field scale. Nevertheless, it provides visual observation of interaction of aqueous/oil/solid phases in micro-scale and helps understand the mechanism of flooding.

CHAPTER VI

SUMMARY

6.1 Summary

Energy demand has been considered as one of the most challenging task in the 21st century. Therefore, it is important to develop more efficient methods or materials from every perspectives.

In the dissertation, 1 D (nanowires and rods) and 2 D (nanodisks) nanomaterials were fabricated via various synthesis routes and applied to energy related applications including photocatalytic hydrogen production and enhanced oil recovery. In **Chapter II**, with appropriate surface treatment, Zn_3P_2 nanowires were not only prevented from degradation, but also able to produce 405 times more of hydrogen. In addition, the deposition of CuO onto TiO_2 rods successfully extend the adsorption from UV to visible light region and subsequently increase photocatalytic activity. In **Chapter III**, we explored several methods to synthesize discotic ZrP nanodisks. New developed microwave-assisted synthesis method could substantially reduce reaction time and precisely control reaction parameters. Finally, in **Chapter IV** and **V**, 2 D ZrP nanodisks tailored with surface modifier were proven to have potential to function as solid surfactant to use in EOR. Besides, microfluidic devices provide microscopic observation of interaction between oil and injected fluid, which is helpful for determination/design of surfactant in EOR.

6.2 Future Research and Ongoing Projects

6.2.1 Microwave-assisted synthesis of magnetic nanodisks and grow "columnar" structure in-situ for study of liquid crystal

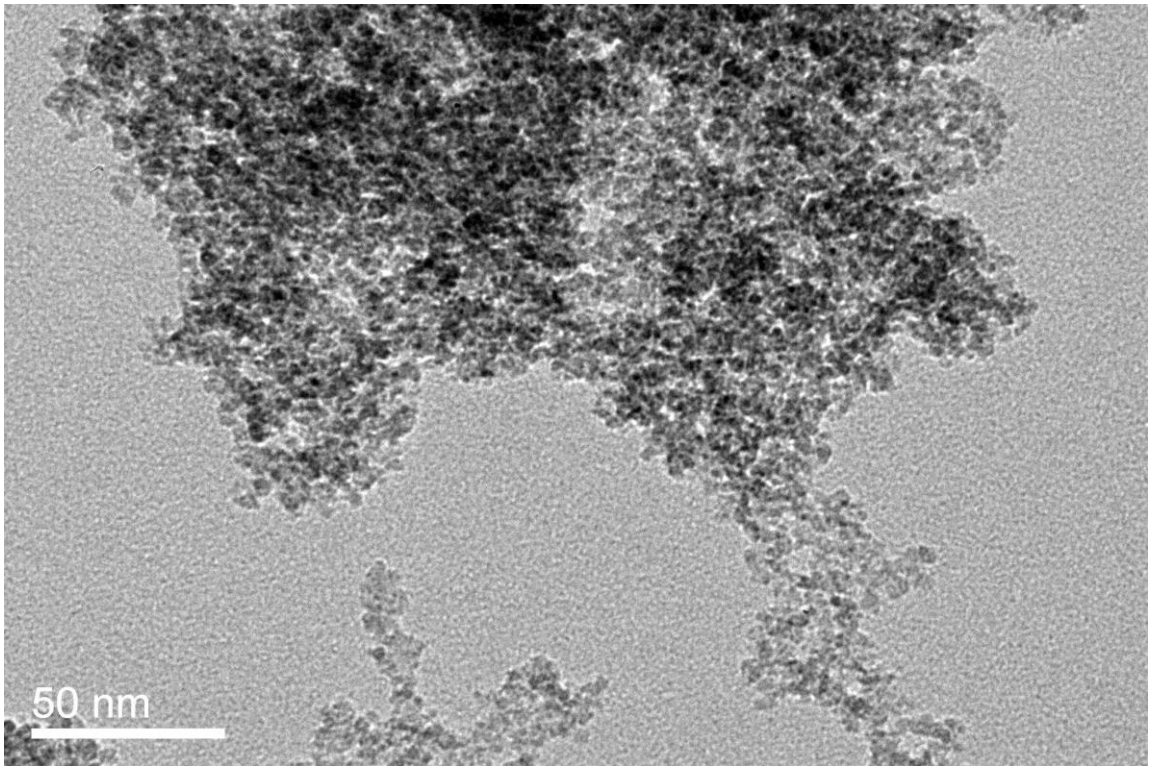

Figure 46. TEM image of $BaFe_{11.5}Sc_{0.5}O_{19}$ colloidal magnetic nanodisks.

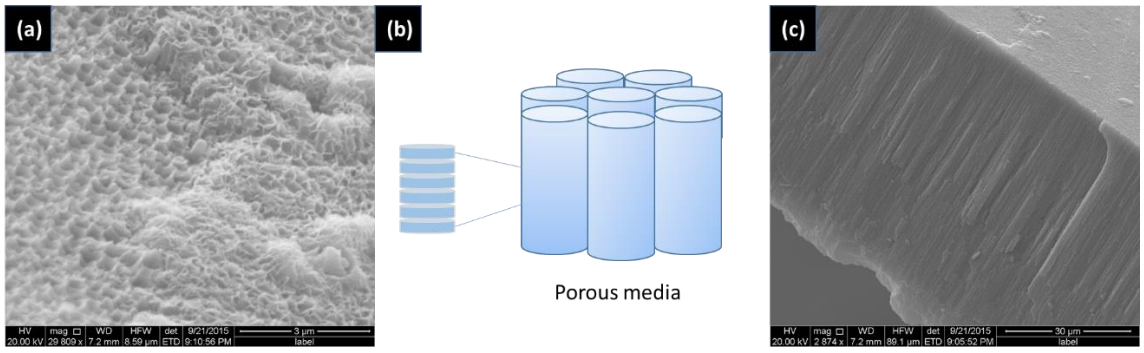

Figure 47. (a) Top-view of ZrP synthesized in-situ in a porous media, (b) schematic illustration of columnar structure of liquid crystal, and (c) side view of ZrP synthesized in-situ in a porous media.

Ferromagnetic nanoparticles is similar to colloidal suspensions, in which their moments can be controlled by applying magnetic field. Efforts have been made to make such suspension macroscopically ferromagnetic in the absence of magnetic field. We plan on using microwave irradiation to synthesize different size of ferromagnetic $BaFe_{11.5}Sc_{0.5}O_{19}$ nanodisks (Figure 46) to study the isotropic-nematic liquid crystal phase transition.

In addition another disk-shape nanomaterial, we also plan on growing ZrP nanodisks in-situ in a porous media to obtain vertically aligned liquid crystal structure (Figure 47). Anodic aluminum oxide (AAO) has been widely used as porous media due to its uniform and self-organized honeycomb structure. The opening size of AAO could be well-controlled in the formation process that could potentially affect the structure of discotic liquid crystal.

6.2.2 Using ZrP nanodisks as surfactants

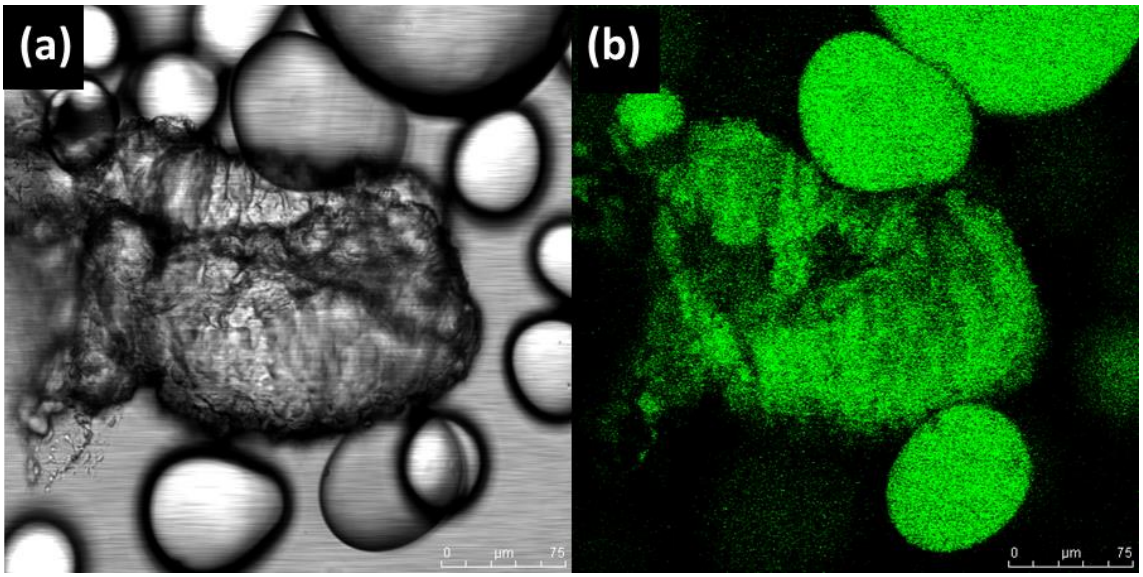

Figure 48. Confocal images of skin-like emulsion (a) optical microscope and (b) fluorescent confocal image.

In the study of ternary system of Janus ZrP/dodecane/water, we found a small window showing non-equilibrium state in ternary phase diagram **(**Figure 48**)**. We proposed that it could be a new route to form bicontinuous interfacially jammed emulsion gels (bijel). Bijels is an emerging class of soft material, in which binary interface of liquids were arrested by nanodisks. It has been predicted by numerical model and confirmed by following experimental work [90]. The curvature of the interface and long range interconnectivity of bijel are desirable for efficient mass transport and heterogeneous catalysis [91]. Pathways to formation of bijel derived from colloidal particles are scarcely reported due to the limitation of privileged pairs of liquids, sophistically preparation of nanoparticles, and limited quench rate. Herein our results report to use simple agitation method to prepare bijel stabilized by Janus ZrP nanopplatelets.

6.2.3 Using better-design microfluidic chip

An intuitive and rapid technology to visualize oil recovery is enabled by microfluidic chip. However, the microfluidic chip used in ***3.3.4*** is with regular network and fixed pillar pitch, which makes it hard to correlate its results to nature rock structure. Our future work is to develop microfluidic chip with a better design whose geometric structure is more similar to nature occurring rock channels. In addition, disk shape of nature minerals, such as laponite, will be surface modified and evaluated for study of EOR. Future work is also needed to study the effects of temperature, salinity, types of crude oil to evaluate the feasibility to use nanomaterials as alternatives of surfactant for EOR.

REFERENCES

(1) J. Conti, P. Holtberg, J. Diefenderfer, A. LaRose, J. T. Turnure, L. Westfall, International Energy Outlook 2016, U.S. Energy Information Administration, 2016.

(2) A. Fujishima, K. Honda, *Photolysis-decomposition of water at the surface of an irradiated semiconductor*, Nature, 1972, **238**, 37-38.

(3) A. Kudo, Y. Miseki, *Heterogeneous photocatalyst materials for water splitting*, Chemical Society Reviews, 2009, **38**, 253-278.

(4) X. Chen, S. Shen, L. Guo, S. S. Mao, *Semiconductor-based photocatalytic hydrogen generation*, Chemical Reviews, 2010, **110**, 6503-6570.

(5) A. Wolcott, W. A. Smith, T. R. Kuykendall, Y. Zhao, J. Z. Zhang, *Photoelectrochemical water splitting using dense and aligned TiO_2 nanorod arrays*, Small, 2009, **5**, 104-11.

(6) K. Nakata, A. Fujishima, *TiO_2 photocatalysis: Design and applications*, Journal of Photochemistry and Photobiology C: Photochemistry Reviews, 2012, **13**, 169-189.

(7) H. Sun, J. Deng, L. Qiu, X. Fang, H. Peng, *Recent progress in solar cells based on one-dimensional nanomaterials*, Energy & Environmental Science, 2015, **8**, 1139-1159.

(8) G. Ramos-Sanchez, M. Albornoz, Y.-H. Yu, Z. Cheng, V. Vasiraju, S. Vaddiraju, F. El Mellouhi, P. B. Balbuena, *Organic molecule-functionalized Zn_3P_2 nanowires for photochemical H_2 production: DFT and experimental analyses*, International Journal of Hydrogen Energy, 2014, **39**, 19887-19898.

(9) I. S. Cho, M. Logar, C. H. Lee, L. Cai, F. B. Prinz, X. Zheng, *Rapid and controllable flame reduction of TiO_2 nanowires for enhanced solar water-splitting*, Nano Letters, 2014, **14**, 24-31.

(10) G. Wang, H. Wang, Y. Ling, Y. Tang, X. Yang, R. C. Fitzmorris, C. Wang, J. Z. Zhang, Y. Li, *Hydrogen-treated TiO_2 nanowire arrays for photoelectrochemical water splitting*, Nano Letters, 2011, **11**, 3026-33.

(11) Z. Zhang, L. Zhang, M. N. Hedhili, H. Zhang, P. Wang, *Plasmonic gold nanocrystals coupled with photonic crystal seamlessly on TiO_2 nanotube photoelectrodes for efficient visible light photoelectrochemical water splitting*, Nano Letters, 2013, **13**, 14-20.

(12) K. Kiatkittipong, A. Iwase, J. Scott, R. Amal, *Photocatalysis of heat treated sodium- and hydrogen-titanate nanoribbons for water splitting, H_2/O_2 generation and oxalic acid oxidation*, Chemical Engineering Science, 2013, **93**, 341-349.

(13) Y. Li, T. Takata, D. Cha, K. Takanabe, T. Minegishi, J. Kubota, K. Domen, *Vertically aligned Ta_3N_5 nanorod arrays for solar-driven photoelectrochemical water splitting*, Advanced Materials, 2013, **25**, 125-31.

(14) M. A. Creighton, Y. Ohata, J. Miyawaki, A. Bose, R. H. Hurt, *Two-dimensional materials as emulsion stabilizers: interfacial thermodynamics and molecular barrier properties*, Langmuir, 2014, **30**, 3687-96.

(15) D. Duonghong, E. Borgarello, M. Graetzel, *Dynamics of light-induced water cleavage in colloidal systems*, Journal of the American Chemical Society, 1981, **103**, 4685-4690.

(16) S.-H. Lee, Y. Park, K.-R. Wee, H.-J. Son, D. W. Cho, C. Pac, W. Choi, S. O. Kang, *Significance of Hydrophilic Characters of Organic Dyes in Visible-Light Hydrogen Generation Based on TiO_2,* Organic Letters, 2009, **12**, 460-463.

(17) C. Xiaobo, *Titanium dioxide nanomaterials and their energy applications*, Chinese Journal of Catalysis, 2009, **30**, 839-851.

(18) L. Brockway, V. Vasiraju, H. Asayesh-Ardakani, R. Shahbazian-Yassar, S. Vaddiraju, *Thermoelectric properties of large-scale Zn_3P_2 nanowire assemblies*, Nanotechnology, 2014, **25**, 145401.

(19) J. M. Pawlikowski, N. Mirowska, P. Becla, *Photoelectric properties of Zn_3P_2*, Solid-State Electronics, 1980, **23**, 755-758.

(20) A. Elmeligi, N. Ismail, *Hydrogen evolution reaction of low carbon steel electrode in hydrochloric acid as a source for hydrogen production*, International Journal of Hydrogen Energy, 2009, **34**, 91-97.

(21) E. A. Sanchez, R. A. Comelli, *Hydrogen production by glycerol steam-reforming over nickel and nickel-cobalt impregnated on alumina*, International Journal of Hydrogen Energy, 2014, **39**, 8650-8655.

(22) P. Mishra, D. Das, *Biohydrogen production from Enterobacter cloacae IIT-BT 08 using distillery effluent*, International Journal of Hydrogen Energy, 2014, **39**, 7496-7507.

(23) S. Yossan, L. Xiao, P. Prasertsan, Z. He, *Hydrogen production in microbial electrolysis cells: Choice of catholyte*, International Journal of Hydrogen Energy, 2013, **38**, 9619-9624.

(24) Y. Sun, K.-P. Yan, *Effect of anodization voltage on performance of TiO_2 nanotube arrays for hydrogen generation in a two-compartment photoelectrochemical cell*, International Journal of Hydrogen Energy, 2014, **39**, 11368-11375.

(25) A. Fujishima, K. Honda, *Electrochemical Photocalysis of Water at A Semiconductor Electrode*, Nature, 1972, **238**, 37-38.

(26) H. Yu, S. Yan, Z. Li, T. Yu, Z. Zou, *Efficient visible-light-driven photocatalytic H_2 production over Cr/N-codoped $SrTiO_3$*, International Journal of Hydrogen Energy, 2012, **37**, 12120-12127.

(27) J. Jiang, M. Wang, R. Li, L. Ma, L. Guo, *Fabricating CdS/$BiVO_4$ and $BiVO_4$/CdS heterostructured film photoelectrodes for photoelectrochemical applications*, International Journal of Hydrogen Energy, 2013, **38**, 13069-13076.

(28) M. Tian, H. Wang, D. Sun, W. Peng, W. Tao, *Visible light driven nanocrystal anatase TiO_2 doped by Ce from sol–gel method and its photoelectrochemical water splitting properties*, International Journal of Hydrogen Energy, 2014, **39**, 13448-13453.

(29) C.-J. Lin, Y.-H. Yu, Y.-H. Liou, *Free-standing TiO_2 nanotube array films sensitized with CdS as highly active solar light-driven photocatalysts*, Applied Catalysis B: Environmental, 2009, **93**, 119-125.

(30) F. Pei, S. Xu, W. Zuo, Z. Zhang, Y. Liu, S. Cao, *Effective improvement of photocatalytic hydrogen evolution via a facile in-situ solvothermal N-doping strategy in N-TiO_2/N-graphene nanocomposite*, International Journal of Hydrogen Energy, 2014, **39**, 6845-6852.

(31) J. Hensel, G. Wang, Y. Li, J. Z. Zhang, *Synergistic effect of CdSe quantum dot sensitization and nitrogen doping of TiO_2 nanostructures for photoelectrochemical solar hydrogen generation*, Nano Letters, 2010, **10**, 478-83.

(32) N. Alenzi, W.-S. Liao, P. S. Cremer, V. Sanchez-Torres, T. K. Wood, C. Ehlig-Economides, Z. Cheng, *Photoelectrochemical hydrogen production from water/methanol decomposition using Ag/TiO_2 nanocomposite thin films*, International Journal of Hydrogen Energy, 2010, **35**, 11768-11775.

(33) M. Ye, J. Gong, Y. Lai, C. Lin, Z. Lin, *High-efficiency photoelectrocatalytic hydrogen generation enabled by palladium quantum dots-sensitized TiO_2 nanotube arrays*, Journal of the American Chemical Society, 2012, **134**, 15720-3.

(34) L. Q. Jiaguo Yu, and Mietek Jaroniec, *Hydrogen Production by Photocatalytic Water Splitting over Pt/TiO_2 Nanosheets with Exposed (001) Facets*, Journal of Physical Chemistry C, 2010, **114**, 13118-13125.

(35) X. Cui, G. Jiang, M. Zhu, Z. Zhao, L. Du, Y. Weng, C. Xu, D. Zhang, Q. Zhang, Y. Wei, A. Duan, J. Liu, J. Gao, *TiO_2/CdS composite hollow spheres with controlled synthesis of platinum on the internal wall for the efficient hydrogen evolution*, International Journal of Hydrogen Energy, 2013, **38**, 9065-9073.

(36) B. Wang, Q. Sun, S. Liu, Y. Li, *Synergetic catalysis of CuO and graphene additives on TiO_2 for photocatalytic water splitting*, International Journal of Hydrogen Energy, 2013, **38**, 7232-7240.

(37) J. M. Kum, S. H. Yoo, G. Ali, S. O. Cho, *Photocatalytic hydrogen production over CuO and TiO_2 nanoparticles mixture*, International Journal of Hydrogen Energy, 2013, **38**, 13541-13546.

(38) W.-T. Chen, V. Jovic, D. Sun-Waterhouse, H. Idriss, G. I. N. Waterhouse, *The role of CuO in promoting photocatalytic hydrogen production over TiO_2*, International Journal of Hydrogen Energy, 2013, **38**, 15036-15048.

(39) M. Bhushan, *Polycrystalline Zn_3P_2 Schottky barrier solar cells*, Applied Physics Letters, 1981, **38**, 39.

(40) L. Brockway, M. Van Laer, Y. Kang, S. Vaddiraju, *Large-scale synthesis and in situ functionalization of Zn_3P_2 and Zn_4Sb_3 nanowire powders*, Physical Chemistry Chemical Physics, 2013, **15**, 6260-6267.

(41) Y. Wang, M. Wu, W. F. Zhang, *Preparation and electrochemical characterization of TiO_2 nanowires as an electrode material for lithium-ion batteries*, Electrochimica Acta, 2008, **53**, 7863-7868.

(42) Y. Xie, S. H. Heo, Y. N. Kim, S. H. Yoo, S. O. Cho, *Synthesis and visible-light-induced catalytic activity of Ag_2S-coupled TiO_2 nanoparticles and nanowires*, Nanotechnology, 2010, **21**, 015703.

(43) C. Guo, J. Xu, Y. He, Y. Zhang, Y. Wang, *Photodegradation of rhodamine B and methyl orange over one-dimensional TiO_2 catalysts under simulated solar irradiation*, Applied Surface Science, 2011, **257**, 3798-3803.

(44) M. Baghbanzadeh, L. Carbone, P. D. Cozzoli, C. O. Kappe, *Microwave-assisted synthesis of colloidal inorganic nanocrystals*, Angewandte Chemie, 2011, **50**, 11312-59.

(45) A. M. Cassell, J. A. Raymakers, J. Kong, H. Dai, *Large Scale CVD Synthesis of Single-Walled Carbon Nanotubes*, The Journal of Physical Chemistry B, 1999, **103**, 6484-6492.

(46) K. S. Kim, Y. Zhao, H. Jang, S. Y. Lee, J. M. Kim, K. S. Kim, J. H. Ahn, P. Kim, J. Y. Choi, B. H. Hong, *Large-scale pattern growth of graphene films for stretchable transparent electrodes*, Nature, 2009, **457**, 706-10.

(47) L. Brockway, M. Van Laer, Y. Kang, S. Vaddiraju, *Large-scale synthesis and in situ functionalization of Zn_3P_2 and Zn_4Sb_3 nanowire powders*, Physical chemistry chemical physics : PCCP, 2013, **15**, 6260-7.

(48) T. Miwa, S. Kaneco, H. Katsumata, T. Suzuki, K. Ohta, S. Chand Verma, K. Sugihara, *Photocatalytic hydrogen production from aqueous methanol solution with $CuO/Al_2O_3/TiO_2$ nanocomposite*, International Journal of Hydrogen Energy, 2010, **35**, 6554-6560.

(49) J. Bandara, C. P. Udawatta, C. S. Rajapakse, *Highly stable CuO incorporated TiO_2 catalyst for photo-catalytic hydrogen production from H_2O*, Photochemical & photobiological sciences : Official journal of the European Photochemistry Association and the European Society for Photobiology, 2005, **4**, 857-61.

(50) T. H. Yu, W. Y. Cheng, K. J. Chao, S. Y. Lu, *$ZnFe_2O_4$ decorated CdS nanorods as a highly efficient, visible light responsive, photochemically stable, magnetically recyclable photocatalyst for hydrogen generation*, Nanoscale, 2013, **5**, 7356-60.

(51) M. Ni, M. K. H. Leung, D. Y. C. Leung, K. Sumathy, *A review and recent developments in photocatalytic water-splitting using TiO_2 for hydrogen production*, Renewable and Sustainable Energy Reviews, 2007, **11**, 401-425.

(52) R. Yang, Y.-L. Chueh, J. R. Morber, R. Snyder, L.-J. Chou, Z. L. Wang, *Single-Crystalline Branched Zinc Phosphide Nanostructures: Synthesis,Properties, and Optoelectronic Devices*, Nano Letters, 2007, **7**, 269-275.

(53) E. J. Luber, M. H. Mobarok, J. M. Buriak, *Solution-Processed Zinc Phosphide (a-Zn_3P_2) Colloidal Semiconducting Nanocrystals for Thin Film Photovoltaic Applications*, AcsNano, 2013, **7**, 8136-8146.

(54) J. S. Jang, U. A. Joshi, J. S. Lee, *Solvothermal Synthesis of CdS Nanowires for Photocatalytic Hydrogen and Electricity Production*, The Journal of Physical Chemistry C, 2007, **111**, 13280-13287.

(55) Q. Li, B. Guo, J. Yu, J. Ran, B. Zhang, H. Yan, J. R. Gong, *Highly efficient visible-light-driven photocatalytic hydrogen production of CdS-cluster-decorated graphene nanosheets*, Journal of the American Chemical Society, 2011, **133**, 10878-84.

(56) Y. Li, Y. Hu, S. Peng, G. Lu, S. Li, *Synthesis of CdS Nanorods by an Ethylenediamine Assisted Hydrothermal Method for Photocatalytic Hydrogen Evolution*, The Journal of Physical Chemistry C, 2009, **113**, 9352-9358.

(57) A. Usuki, N. Hasegawa, M. Kato, *Polymer-Clay Nanocomposites*, Advances in Polymer Science, 2005, **179**, 135-195.

(58) K. Varoon, X. Zhang, B. Elyassi, D. D. Brewer, M. Gettel, S. Kumar, J. A. Lee, S. Maheshwari, A. Mittal, C.-Y. Sung, M. Cococcioni, L. F. Francis, A. V. McCormick, K. A. Mkhoyan, M. Tsapatsis, *Dispersible Exfoliated Zeolite Nanosheets and Their Application as a Selective Membrane*, Science, 2011, **334**, 72-75.

(59) A. F. Mejia, Y.-W. Chang, R. Ng, M. Shuai, M. Sam Mannan, Z. Cheng, *Aspect ratio and polydispersity dependence of isotropic-nematic transition in discotic suspensions*, Physical Review E, 2012, **85**, 061708(1-12).

(60) S. A. F. Bon, P. J. Colver, *Pickering Miniemulsion Polymerization Using Laponite Clay as a Stabilizer*, Langmuir, 2007, **23**, 8316-8322.

(61) A. Clearfield, J. A. Stynes, *The preparation of crystalline zirconium phosphate and some observations on its ion exchange behaviour*, Journal of Inorganic and Nuclear Chemistry, 1964, **26**, 117-129.

(62) M. Shuai, A. F. Mejia, Y.-W. Changa, Z. Cheng, *Hydrothermal synthesis of layered α-zirconium phosphate disks: control of aspect ratio and polydispersity for nano-architecture*, CrystEngComm, 2013, **15**, 1970-1977.

(63) L. Sun, W. J. Boo, H.-J. Sue, A. Clearfield, *Preparation of α-zirconium phosphate nanoplatelets with wide variations in aspect ratios*, New Journal of Chemistry, 2007, **31**, 39-43.

(64) Manoj B. Gawande, Sharad N. Shelke, Radek Zboril, R. S. Varma, *Microwave-Assisted Chemistry: Synthetic Applications for Rapid Assembly of Nanomaterials and Organics*, Accounts of Chemical Research, 2014, **47**, 1338-1348.

(65) Y.-W. Chang, A. F. Mejia, Z. Cheng, X. Di, G. B. McKenna, *Gelation via Ion Exchange in Discotic Suspensions*, Physical Review Letters, 2012, **108**, 247802(1-5).

(66) X. Wang, D. Zhao, A. Diaz, I. B. Nava Medina, H. Wang, Z. Cheng, *Thermo-sensitive discotic colloidal liquid crystals*, Soft Matter, 2014, **120**, 7692-7695.

(67) M. Wong, R. Ishige, K. L. White, P. Li, D. Kim, R. Krishnamoorti, R. Gunther, T. Higuchi, H. Jinnai, A. Takahara, R. Nishimura, H.-J. Sue, *Large-scale self-assembled zirconium phosphate smectic layers via a simple spray-coating process*, Nature Communications, 2014, **5**, 3589(1-12).

(68) M. Chen, H. Li, Y. Chen, A. F. Mejia, X. Wang, Z. Cheng, *Observation of isotropic–isotropic demixing in colloidal platelet–sphere mixtures*, Soft Matter, 2015, **11**, 5775-5779.

(69) D. Sun, H.-J. Sue, Z. Cheng, Y. Martínez-Ratón, E. Velasco, *Stable smectic phase in suspensions of polydisperse colloidal platelets with identical thickness*, Physical Review E, 2009, **80**, 041704(1-6).

(70) A. Diaz, V. Saxena, J. Gonzalez, A. David, B. Casanas, C. Carpenter, J. D. Batteas, J. L. Colon, A. Clearfield, M. D. Hussain, *Zirconium phosphate nano-platelets: a novel platform for drug delivery in cancer therapy*, Chemical Communications, 2012, **48**, 1754-1756.

(71) H.-N. Kim, S. W. Keller, T. E. Mallouk, *Characterization of Zirconium Phosphate/Polycation Thin Films Grown by Sequential Adsorption Reactions*, Chemistry of Materials, 1997, **9**, 1414–1421.

(72) M. Shuai, A. F. Mejia, Y.-W. Changa, Z. Cheng, *Hydrothermal synthesis of layered α-zirconium phosphate disks: control of aspect ratio and polydispersity for nano-architecture*, CrystEngComm, 2013, **15**, 1970.

(73) A. Clearfield, G. D. Smith, *Crystallography and structure of alpha-zirconium bis(monohydrogen orthophosphate) monohydrate*, Inorganic Chemistry, 1969, **8**.

(74) R. Backov, B. Bonnet, D. J. Jones, J. Rozie, *Assembly of Partially Oxidized Tetrathiafulvalene in Layered Phosphates. Formation of Conducting Organic-Inorganic Hybrids by Intercalation*, Chemistry of Materials, 1997, **9**, 1812-1818.

(75) A. Diaz, V. Saxena, J. Gonzalez, A. David, B. Casanas, C. Carpenter, J. D. Batteas, J. L. Colon, A. Clearfield, M. D. Hussain, *Zirconium phosphate nano-platelets: a novel platform for drug delivery in cancer therapy*, Chemical Communications, 2012, **48**, 1754-6.

(76) J. S. Guevara, A. F. Mejia, M. Shuai, Y.-W. Chang, M. S. Mannan, Z. Cheng, *Stabilization of Pickering foams by high-aspect-ratio nano-sheets*, Soft Matter, 2013, **9**, 1327-1336.

(77) F. Carn, A. Derré, W. Neri, O. Babot, H. Deleuze, R. Backov, *Shaping zirconium phosphate α-Zr(HPO4)2·H2O: from exfoliation to first α-ZrP 3D open-cell macrocellular foams*, New Journal of Chemistry, 2005, **29**, 1346.

(78) A. F. Mejia, A. Diaz, S. Pullela, Y.-W. Chang, M. Simonetty, C. Carpenter, J. D. Batteas, M. S. Mannan, A. Clearfield, Z. Cheng, *Pickering emulsions stabilized by amphiphilic nano-sheets*, Soft Matter, 2012, **8**, 10245.

(79) L. Sun, W. J. Boo, H.-J. Sue, A. Clearfield, *Preparation of α-zirconium phosphate nanoplatelets with wide variations in aspect ratios*, New Journal of Chemistry, 2007, **31**, 39-43.

(80) H. Li, X. Wang, Y. Chen, Z. Cheng, *Temperature-dependent isotropic-to-nematic transition of charged nanoplates*, Physical Review E, 2014, **90**.

(81) M. B. Gawande, S. N. Shelke, R. Zboril, R. S. Varma, *Microwave-assisted chemistry: synthetic applications for rapid assembly of nanomaterials and organics*, Accounts of Chemical Research, 2014, **47**, 1338-48.

(82) S. U. Pickering, *Emulsion CXCVI*, Journal of the Chemical Society, 1907, **91**, 2001-2021.

(83) E. Dickinson, *Food emulsions and foams: Stabilization by particles*, Current Opinion in Colloid & Interface Science, 2010, **15**, 40-49.

(84) J. Sun, H. Bi, *Pickering emulsion fabrication and enhanced supercapacity of graphene oxide-covered polyaniline nanoparticles*, Materials Letters, 2012, **81**, 48-51.

(85) M. F. Haase, D. Grigoriev, H. Moehwald, B. Tiersch, D. G. Shchukin, *Encapsulation of Amphoteric Substances in a pH-Sensitive Pickering Emulsion*, Journal of Physical Chemistry C, 2010, **114**, 17304-17310.

(86) J. Frelichowska, M. A. Bolzinger, J. Pelletier, J. P. Valour, Y. Chevalier, *Topical delivery of lipophilic drugs from o/w Pickering emulsions*, International Journal of Pharmaceutics, 2009, **371**, 56-63.

(87) T. W. de Haas, H. Fadaei, U. Guerrero, D. Sinton, *Steam-on-a-chip for oil recovery: the role of alkaline additives in steam assisted gravity drainage*, Lab on a Chip, 2013, **13**, 3832-9.

(88) K. Ma, R. Liontas, C. A. Conn, G. J. Hirasaki, S. L. Biswal, *Visualization of improved sweep with foam in heterogeneous porous media using microfluidics*, Soft Matter, 2012, **8**, 10669.

(89) M. Pica, A. Donnadio, D. Capitani, R. Vivani, E. Troni, M. Casciola, *Advances in the chemistry of nanosized zirconium phosphates: a new mild and quick route to the synthesis of nanocrystals*, Inorganic Chemistry, 2011, **50**, 11623-30.

(90) K. Stratford, R. Adhikari, I. Pagonabarraga, J.-C. Desplat, M. E. Cates, *Colloidal Jamming at Interfaces: A Route to Fluid-Bicontinuous Gels*, Science, 2005, **309**, 2198-2201.

(91) K. A. Rumble, J. H. Thijssen, A. B. Schofield, P. S. Clegg, *Compressing a spinodal surface at fixed area: bijels in a centrifuge*, Soft Matter, 2016, **12**, 4375-83.

APPENDIX

PEER-REVIEWED PUBLICATIONS

This dissertation is based on the following publications:

1. **Yu, Y.H.**, Wang, X., Shinde, A., Cheng, Z., "*Synthesis and exfoliation of discotic zirconium phosphate to obtain colloidal liquid crystals*", Journal of Visualized Experiments, doi:10.3791/53511 (2016) e53511.
2. **Yu, Y.H.**, Chen, Y.P., Cheng, Z., "*Microwave-assisted rapid synthesis of hexagonal α-zirconium phosphate nanodisks as a Pickering emulsion stabilizer*", Materials Letters, 163 (2016) 158-161
3. **Yu, Y.H.**, Chen, Y.P., Cheng, Z., "*Rapid Facile Microwave-assisted Solvothermal Synthesis of Rod-like CuO/TiO_2 for High-efficiency Photocatalytic Hydrogen Evolution*", International Journal of Hydrogen Energy, 40 (2015) 15994-16000.
4. Li, H, **Yu, Y.H.**, Vasiraju, V, Vaddiraju S, Cheng Z., "*Investigation of Electron Transport Through Alkanedithoil of Functionalized Zn_3P_2 Nanowires for Hydrogen Production*", International Journal of Nano Studies & Technology, (2016) S1:001, 1-5.
5. Ramos-Sanchez, G., Albornoz, M., **Yu, Y.H.**, Cheng, Z., Vasiraju, V., Vaddiraju, S., El Mellouhi, F., Balbuena, P.B. "*Organic molecule-functionalized Zn_3P_2 nanowires for photochemical H_2 production: DFT and experimental analyses*", International Journal of Hydrogen Energy, 39 (2014) 19887-19898.

Other papers by the author:

1. Shinde, A., Wang, X., **Yu, Y.H.**, Cheng Z., "*Aspect ratio dependence of isotropic-nematic phase separation of nanoplates in gravity*", Gravity and Space Research Journal, 4 (2016) 17-26
2. Zeng, M., Wang, X., **Yu, Y.H.**, Zhang, L., Shafi, W., Huang, X. and Cheng, Z. "*The Synthesis of Amphiphilic Luminescent Graphene Quantum Dot and Its Application in Mini-Emulsion Polymerization*", Journal of Nanomaterials, vol. 2016, 6490383, (2016) doi:10.1155/2016/6490383.
3. Wang, X., Zhang, L., **Yu, Y.H.**, Jia, L., Sam Mannan, M., Chen, Y., Cheng, Z., "*Nano-encapsulated PCM via Pickering Emulsification*", Scientific Reports, 5, (2015) 13357